JGR Oceans

RESEARCH ARTICLE
10.1029/2021JC017720

The Evolution of a Northward-Propagating Buoyant Coastal Plume After a Wind Relaxation Event

Jacqueline M. McSweeney[1], Melanie R. Fewings[1], James A. Lerczak[1], and John A. Barth[1]

[1]College of Earth, Ocean, and Atmospheric Sciences, Oregon State University, Corvallis, OR, USA

Key Points:

- After a wind relaxation, there are two northward propagating signals: an alongshore velocity signal (~0.7 m/s) and a warm signal (~0.2 m/s)
- The warm buoyant plume becomes cooler and thinner as it propagates alongshore, resulting in a weakening of the cross-front temperature difference
- The nonuniform propagation velocity of the warm plume is not explained by tidal advection or plume cooling

Correspondence to:
J. M. McSweeney,
jack.mcsweeney@oregonstate.edu

Citation:
McSweeney, J. M., Fewings, M. R., Lerczak, J. A., & Barth, J. A. (2021). The evolution of a northward-propagating buoyant coastal plume after a wind relaxation event. *Journal of Geophysical Research: Oceans*, *126*, e2021JC017720. https://doi.org/10.1029/2021JC017720

Received 29 JUN 2021
Accepted 7 NOV 2021

Abstract After a relaxation of the regional southward, upwelling-favorable winds along the central California coast, warm water from the Santa Barbara Channel propagates northward as a buoyant plume. As the plume transits up the coast, it causes abrupt temperature changes and modifies shelf stratification. We use temperature and velocity data from 35 moorings north of Pt. Arguello to track the evolution of a buoyant plume after a wind relaxation event in October 2017. The moorings were deployed September–October 2017 and span a ~30 km stretch of coastline, including nine cross-shelf transects that range from 17 to 100 m water depth. The high spatial resolution of the data set enables us to track the spatiotemporal evolution of the plume, including across-front temperature difference, cross-shore structure, and propagation velocity. We observe an alongshore current velocity signal that takes ~10 hr to propagate ~25 km alongshore (~0.7 m/s) and a temperature signal that takes ~34 hr to propagate the same distance (~0.2 m/s). The plume cools as it transits northward, leading to a decrease in the cross-front temperature difference and the reduced gravity (g'). The plume's propagation velocity is nonuniform in space and time, with accelerations and decelerations unexplained by the alongshore reduction in g' or advection by tidal currents. As the plume reaches the northernmost part of the mooring array, its temperature variability is obscured by internal waves, a prominent feature in the region. We focus on one relaxation event but observe five other similar events over the 2 months record.

Plain Language Summary Coastal ocean conditions along the US west coast are affected by strong, regional-scale winds that predominantly blow southward along California. Under "normal" conditions, these winds and other ocean processes cause a large difference between water temperature in the Santa Barbara Channel (warm) and outside the channel to the northwest (cold). When the regional winds weaken, warm water exits the channel as a buoyant plume and moves northward up the coast. Similar plumes occur elsewhere around the world, and these plumes have important ecological impacts because they transport larvae of coastal marine species. Using instruments in the water at 35 sites north of Pt. Arguello, we study how warm plumes travel along a ~30 km stretch of coastline. Six of these northward-propagating warm plumes were observed September–October 2017, and we primarily describe one event in detail. We study the speed the warm plume travels, how that speed changes in space and time, and why the speed is not constant. We observe that the plume water cools as it moves northward, resulting in increased difficulty identifying the plume in the northern sites. We also find that the plume's warm signature can be obscured by similar warm signals caused by the tides.

1. Introduction

In eastern boundary current systems where regional winds are predominantly upwelling favorable, a wind relaxation often generates a warm, buoyant plume that propagates poleward. These events have been observed worldwide, including along the coasts of northern (Kosro 1987; Send et al., 1987) and central (Melton et al., 2009; Suanda et al., 2016; Washburn et al., 2011) California, near Cape São Vicente (García-Lafuente et al., 2006; Garel et al., 2016; Júnior et al., 2021; Relvas & Barton, 2002, 2005) and the Bay of Biscay (Kersalé et al., 2016) along the Iberian Peninsula, and off the southern Namaqua shelf on the west coast of South Africa (Fawcett et al., 2008). These buoyant poleward flows transport larvae along-coast, affecting recruitment and settlement of invertebrate species (Dudas et al., 2009; Wing et al., 1995, 2003). Since the fate of larvae is also influenced by processes such as internal waves and upwelling that generate cross-shore transport (Garwood et al., 2020; Pineda, 1991; Shanks & Shearman, 2009), it is challenging to decipher the specific ecosystem impacts of warm plumes generated by wind relaxations. In this paper, we study the evolution of warm buoyant plumes that originate from the Santa Barbara Channel and are thought to influence larval transport within the central and southern California ecosystem.

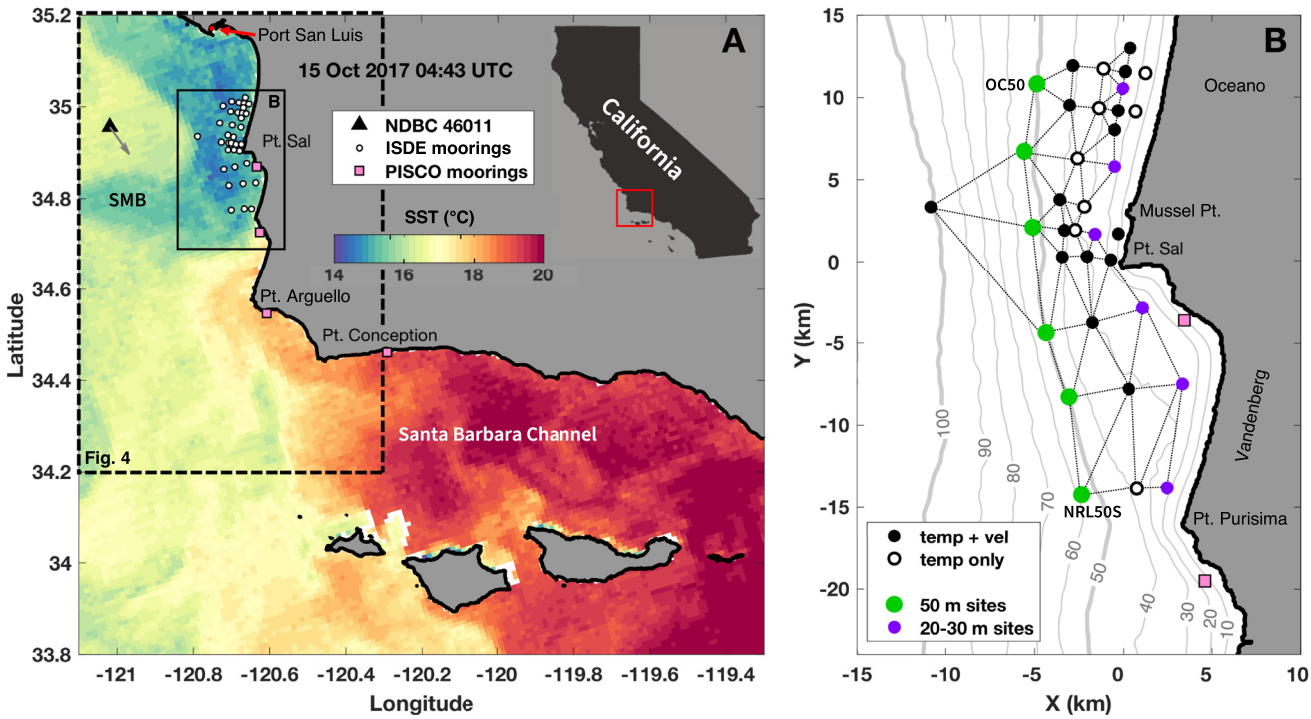

Figure 1. (a) A broad regional map, encompassing part of the Santa Maria Basin (SMB) and the Santa Barbara Channel and including four Partnership for Interdisciplinary Studies of Coastal Oceans (PISCO) mooring locations (pink squares) from previous studies (Melton et al., 2009; Suanda et al., 2016; Washburn et al., 2011), the NDBC buoy used in this analysis (46011, black triangle), and the footprint of the Inner Shelf Dynamics Experiment (ISDE) moorings (small white dots, solid black box). The major principal axis direction of the 33 hr low-pass filtered wind stress at buoy 46011 is denoted by the gray arrow. Sea surface temperature (SST) data from the AVHRR MetOp-B satellite (EUMETSAT, 2020; details provided in Section 2.1) are shown in color for October 15, 2017 04:43 UTC. (b) Zoom-in of the ISDE study site, including the 35 moorings described in Section 2. Gray contours indicate the isobaths, with the water depths labeled in m. Filled circles denote sites with temperature and velocity data, whereas open circles are sites with only temperature data. Large green dots indicate sites along the 50 m isobath, and purple dots are sites of approximately equivalent latitude on the 20–30 m isobaths. Thin dashed black lines indicate the mooring groupings that are used for the frontal propagation velocity estimations discussed in Section 2.2.2.

The Santa Maria Basin (SMB) and the Santa Barbara Channel (SBC) are dynamically distinct regions within the southern central California coast that are physically separated by Pt. Conception (Figure 1). North of Pt. Conception, the regional coastline is oriented north-south and the regional winds are predominantly southeastward and upwelling favorable (Dorman & Winant, 2000). Long-term average currents in the SMB are equatorward over the mid-shelf, but are weakly poleward on the inner shelf due to the influences of episodic flow reversals (Cudaback et al., 2005). South of Pt. Conception, the coastline is oriented east-west. Circulation in the SBC is complex and influenced by a combination of processes, including regional and local winds, along-shelf pressure gradients, and topographic effects (Aristizábal et al., 2017; Cudaback et al., 2005; Fewings et al., 2015; Hendershott & Winant, 1996; Oey et al., 2004).

When the regionally upwelling-favorable winds northwest of Pt. Conception relax, the alongshore currents within a few 10 s of km of the coast flow poleward and warm water from the Santa Barbara Channel can propagate northward into the SMB as a buoyant plume (Melton et al., 2009; Suanda et al., 2016; Washburn et al., 2011). Wind relaxations occur year-round, but are predominate May–November and most frequent in September (Melton et al., 2009). On average, wind relaxations occur every 1–2 weeks and persist for several days (Fewings et al., 2016; Melton et al., 2009). The longevity and eventual poleward extent of a given poleward-propagating warm plume depends on the duration of the wind relaxation and the magnitude of the along shelf temperature and pressure gradients preceding the event (Melton et al., 2009). After a wind relaxation, the inner-shelf velocity field quickly adjusts to a change in the alongshore barotropic pressure gradient and then it typically takes approximately 0.7, 1.8, and 2.6 days for the warm plume to reach Pt. Arguello, Pt. Purisima, and Pt. Sal respectively, though not all plumes reach as far as Pt. Sal (Melton et al., 2009). Analyses of plume occurrences from multi-year datasets have revealed that the SMB plumes can propagate alongshore at speeds ranging from 0.04 to 0.46 m/s and

cause abrupt temperature changes at the plume front ~O(1°–5°C) (Melton et al., 2009; Washburn et al., 2011). Modeling studies have additionally suggested that the plume water tends to intersect the bottom near the ~30 m isobath, with a surface expression extending farther offshore (Suanda et al., 2016).

Compared to fresh water plumes generated from estuarine outflows, thermally buoyant plumes such as those originating from the SBC have smaller density contrasts relative to the ambient water. For example, the Chesapeake Bay outflow plumes have a density difference ($\Delta\rho$) of ~2–3 kg m^{-3} (Lentz et al., 2003) whereas the warm plumes from the SBC typically have a $\Delta\rho$ of ~0.1–0.9 kg m^{-3} (Washburn et al., 2011). Coastal buoyant plume theory distinguishes between slope-controlled plumes, where bottom friction is dynamically important, and surface-trapped plumes, which are minimally influenced by bottom topography (Chapman & Lentz, 1994; Lentz & Helfrich, 2002; Yankovsky & Chapman, 1997). These SBC/SMB warm plumes are in an intermediate parameter space where bottom friction is somewhat dynamically important (Suanda et al., 2016; Washburn et al., 2011). Though the poleward propagation of warm plumes following regional wind relaxations has been observed in eastern boundary upwelling systems globally (Fawcett et al., 2008; García-Lafuente et al., 2006; Júnior et al., 2021; Relvas & Barton, 2005; Woodson et al., 2009), thermal plumes have received relatively little attention compared to freshwater plumes from river outflows and are less well understood than buoyant plumes with larger density contrasts.

Poleward propagating thermal plumes contribute to temperature and stratification variability on the inner continental shelf, but inner-shelf conditions are also influenced by other processes with similar spatial and temporal scales. For example, remotely and locally generated internal tides influence the SMB region and propagate shoreward across the shelf roughly every 6 hr (Colosi et al., 2018; McSweeney, Lerczak, Barth, Becherer, Colosi, et al., 2020; McSweeney, Lerczak, Barth, Becherer, MacKinnon, et al., 2020). The coastline also features several headlands, which can introduce semidiurnal temperature variability nearshore (Feddersen et al., 2020). These other processes are important to consider when investigating plume dynamics on an event scale.

Here, we use water temperature and velocity data from moorings deployed September–October 2017 off the coast of southern central California to investigate the evolution of an alongshore propagating warm plume after a regional wind relaxation event. Previous studies of buoyant plumes in this area (Melton et al., 2009; Suanda et al., 2016; Washburn et al., 2011) have relied on data from moorings spaced ~15–20 km apart alongshore, including only 3 inner shelf sites at ~15 m water depths between Pt. Arguello and Pt. Sal (Figure 1, PISCO data). In contrast, this study leverages a highly spatially resolved data set from the Inner Shelf Dynamics Experiment (ISDE; Kumar et al., 2021; Lerczak et al., 2019), which spans a ~30 km stretch of coastline and includes 35 moorings with nine cross-shelf mooring arrays. The spatiotemporal resolution of the measurements provides a unique opportunity to better understand the dynamic nature of poleward-propagating, thermally buoyant plumes and their effect on local stratification and temperature variability. We investigate the evolution of the plume front structure, the diminishing temperature anomaly as the plume transits north, and the heterogeneity of the plume's frontal propagation speed.

2. Methods

2.1. Observations and Data Processing

The ISDE study site is located between Pt. Purisima and Port San Luis, north of Pt. Arguello (Figure 1). Our observational period is optimal to study poleward flows that follow wind relaxation events because (a) these events occur most frequently in the fall season (Melton et al., 2009) and (b) the freshwater inputs are minimal in the fall (McPhee-Shaw et al., 2007). The 35 moorings used in this analysis are from sites that were spaced 1–5 km apart horizontally and spanned 17–100 m water depth. Most moorings included both temperature and velocity data, with a vertical resolution of 1–2 m and sampling rates ranging from 10 to 60 s. More details about these measurements can be found in McSweeney, Lerczak, Barth, Becherer, Colosi, et al. (2020), McSweeney, Lerczak, Barth, Becherer, MacKinnon, et al. (2020).

The temperature and velocity data at each mooring were processed as in McSweeney, Lerczak, Barth, Becherer, Colosi, et al. (2020), McSweeney, Lerczak, Barth, Becherer, MacKinnon, et al. (2020). To briefly summarize, the data were extrapolated (using a quadratic polynomial regression and assuming no shear at the boundaries) to the surface and seabed in a surface-following, sigma coordinate system (sigma = z/H, where z is the vertical coordinate and H is water depth). For the velocities, data were missing in the top ~10% of the water column because

of sidelobe contamination and in the 1.5 m above the seabed. For the temperature data, there were measurements at 1–2 m increments through the water column but no data in the uppermost 0.5–2 m or bottom 0.5 m. Temporal gaps <5 min were filled by linear interpolation, and then the data were averaged to 1-min resolution. For this analysis, the velocity data were rotated into the principal axis coordinates of the depth-mean subtidal (33 hr low-pass filtered) current at each location so that the coordinate system at each mooring is approximately alongshore (the major principal axis) and across-shore, with positive values corresponding with approximately northward and onshore currents. To evaluate surface conditions, we average temperature data over the top 10 m and velocity data over the top 15% of the water column at each mooring. These differing averaging techniques were used to account for the differences in data coverage over the length of the water column. From here on, "surface" data refers to these averaged data.

Data from the National Data Buoy Center (NDBC) buoy 46011 (Figure 1a) were used for characterizing the regional wind conditions. The wind stress was calculated from the buoy data using the COARE algorithm (v3.6; Edson et al., 2013). We rotated the hourly wind stress data to the principal axis of the 33 hr low-pass filtered data, such that the major axis direction is positive for winds blowing toward the southeast (as shown in Figure 1a). Wind relaxation events were identified following the procedure established by Melton et al. (2009), which entails an empirical orthogonal function (EOF) analysis of wind velocity data from multiple buoys in the region.

To provide regional temperature context, we used ∼1 km resolution sea surface temperature (SST) satellite data. The data is a Group for High Resolution Sea Surface Temperature (GHRSST) Level 2P data set from the Advanced Very High Resolution Radiometer (AVHRR) on the European Meteorological Operational-B (MetOp-B) satellite (EUMETSAT, 2020). For this analysis, we plot only data with a quality level flag of 5, the highest quality.

2.2. Data Analysis

Over the 2-month observational period, there were four regional wind relaxation events identified by the Melton et al. (2009) index: (a) September 11, 2017 02:00, (b) September 26, 2017 20:00, (c) October 9, 2017 06:00, and (d) October 14, 2017 16:00 UTC. However, as discussed further in Section 3c, there are other wind relaxations that do not meet the Melton et al. (2009) criteria but are followed by a warm plume propagating through the observational region. Our in-depth plume evolution analysis focuses on the plume following the 14 October relaxation event.

2.2.1. Identifying the Plume Arrival

Our analyses necessitate the identification of the plume arrival at each mooring. To illustrate our plume identification methods, we show data from NRL50S, the southernmost mooring site, before and after the October 14th relaxation event (Figure 2). After the wind relaxation, two signals propagate north into the mooring array: a northward alongshore velocity signal (Figure 2e) and a warm temperature signal associated with the buoyant plume (Figure 2c). We identify the two signals separately.

To define the arrival of the velocity signal, we identify the time when the 6 hr low-pass filtered surface alongshore velocity becomes northward/positive (Figure 2g). For the arrival identification of the warm signal, we use the 6 hr low-pass filtered surface temperature and flag the fastest increase in temperature (i.e., the peak in $\partial T/\partial t$). The 6 hr filter cutoff was selected to minimize the effects of high-frequency internal waves but preserve the sharp feature associated with the plume front. As discussed further in Section 4.2, these identification methods involve greater uncertainty in shallower water and in the northern part of the study region. We tested a number of identification criteria and confirmed that the findings below are qualitatively insensitive to the various methods.

2.2.2. Estimating Plume Front Propagation Velocities

We track the thermal plume front by linearly interpolating the plume arrival time between sites and calculate the frontal velocity using a triangulation method similar to that used in Scotti et al. (2005) and McSweeney, Lerczak, Barth, Becherer, Colosi, et al. (2020). Using mooring groups of three or four (shown in Figure 1b), we assume the plume transits through each mooring group as a linear feature with constant speed and direction. The speed and direction are then estimated by minimizing the root-mean-squared difference between the best-fit and observed arrival times. Since this estimation of plume frontal propagation velocity relies directly on the arrival times at each mooring, there is greater uncertainty when the identified arrival times are less certain (Section 4.2).

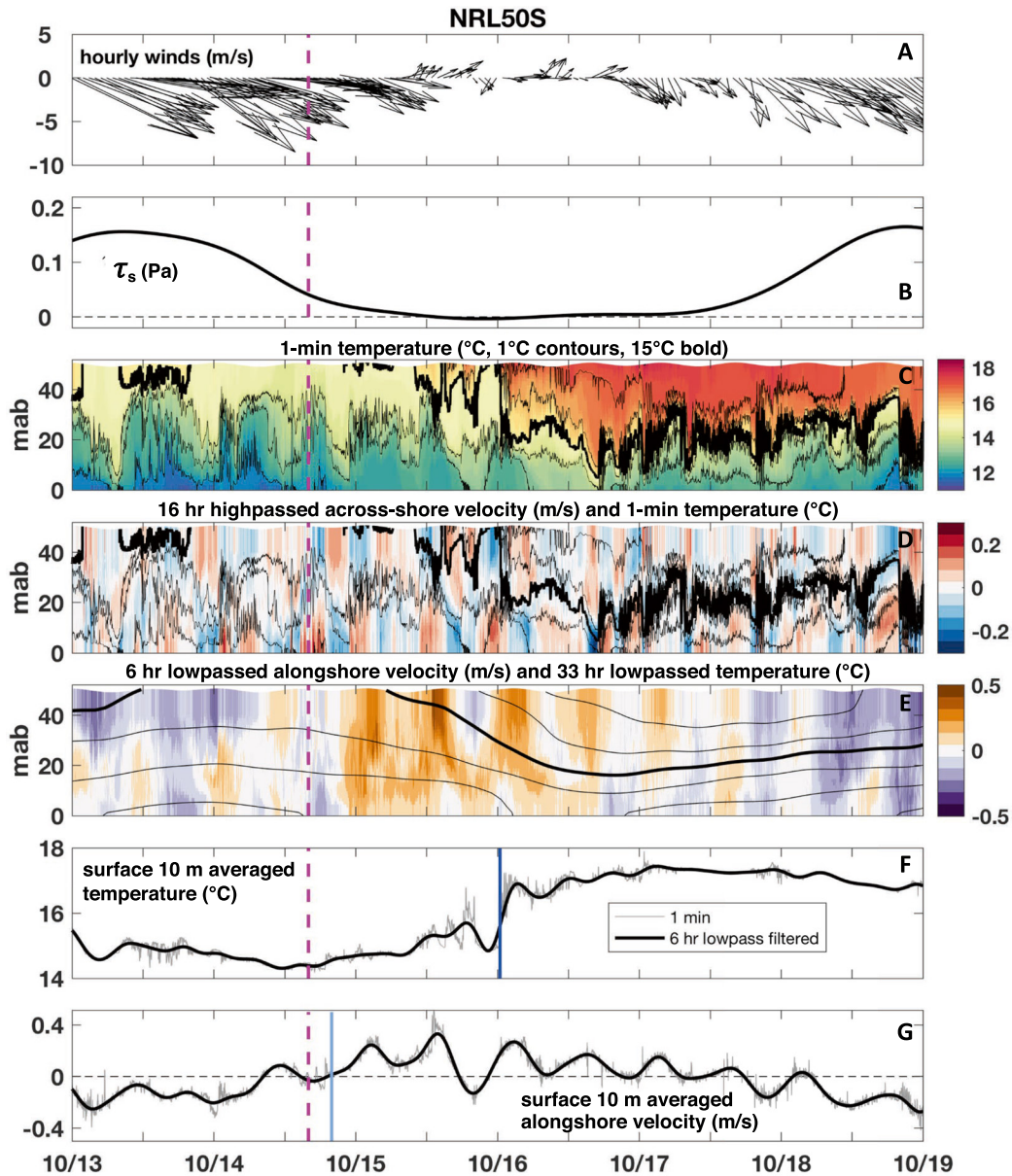

Figure 2. For the 14 October regional wind relaxation event, the hourly wind velocity shown with north upward (a) and the major principal axis component of the 33 hr low-pass filtered wind stress (b, positive towards the southeast) from the 46011 NDBC buoy. The time of each wind relaxation identified by the Melton et al. (2009) index is indicated by the vertical dashed magenta line in the panels. Also, data from the NRL50S mooring, including: (c) 1-min unfiltered temperature data (1°C contours, 15°C isotherm bold), (d) 16 hr high-pass filtered across-shore velocities (colored, positive values shoreward) and 1-min temperature data (black, 1°C contour intervals, 15°C isotherm bold), (e) 6 hr low-pass filtered alongshore velocities (colored, positive values approximately northward) and 33 hr low-pass filtered temperature data (black, 1°C contour intervals, 15°C contour bold), (f) 1-min (gray) and 6 hr low-pass filtered (black) surface temperature, and (g) 1 min (gray) and 6 hr low-pass filtered (black) surface alongshore velocities ("surface" defined in Section 2.1). For c-e, mab is meters above the bed. The vertical blue lines in panels f and g indicate the arrival times identified for the temperature and velocity signals, respectively, associated with the buoyant warm water plume.

We also compute theoretical propagation speeds based on existing theory of buoyant plume propagation (Lentz & Helfrich, 2002). In this framework, the propagation speed (c_p) of a buoyancy front propagating along an alongshore uniform continental shelf with a sloping bottom is:

$$c_p = \frac{c_w}{1 + \frac{c_w}{c_\alpha}} \tag{1}$$

where c_w is the propagation speed in the limit of a large bottom slope

$$c_w = \left(g' h_p\right)^{1/2} \tag{2}$$

and c_α is the propagation speed in the limit of small bottom slope.

$$c_\alpha = \frac{\theta g'}{f} \tag{3}$$

Here, g' is the reduced gravity,

$$g' = g\frac{\rho - \rho_o}{\rho_o} \tag{4}$$

that we estimate from our data such that ρ is the average density within the plume, ρ_o is the density averaged over the 12–36 hr prior to the identified plume arrival, and g is the acceleration due to gravity. In Equation 2, h_p is the depth at which the plume's offshore boundary intersects the sloping topography. In our analysis, we define h_p as the estimated depth at which the 15°C isotherm from the 33 hr low-pass filtered temperature intersects the sea floor, which we estimate to be ~30–35 m (Section 3.2.1). In Equation 3, θ is the bottom slope and f is the Coriolis parameter. In our calculations, we consider both an alongshore-variable θ and a regionally-averaged θ value of 6.6×10^{-3} (McSweeney, Lerczak, Barth, Becherer, MacKinnon, et al., 2020).

3. Results

3.1. Conditions During the Experiment

Regional wind and oceanic conditions varied substantially over the 2-month observational period. The wind predominantly blew towards the southeast, with the 33 hr low-pass filtered wind stress (major principal axis) ranging from 0 to 0.3 Pa (Figure 3a). There were ~$O(10)$ events where the wind stress was near zero, four of which were defined as regional wind relaxations by the criteria defined in Melton et al. (2009). 33 hr low-pass filtered water current velocities at NRL50S reveal a subtidal oceanic circulation characterized by an evolving alongshore flow that reversed directions on timescales of a few days (Figure 3b) and a mostly 3-layer cross-shore flow (Figure 3c).

Timeseries of the 33 hr low-pass filtered surface temperature data from the 50 m moorings displayed several notable patterns (Figure 3d). First, the surface temperature is modulated on timescales of weeks, with generally warmer temperatures in early September and temperature peaks following select wind relaxation events. Second, the magnitude and sign of the alongshore gradient in surface temperature varies throughout the record. Generally, the southern part of the region is warmer than the northern, but sometimes the opposite is true (e.g., 16 September and 22 October) and sometimes there is not a distinct alongshore temperature gradient (e.g., 12 and 26 September). Finally, after some periods of decreased wind stress, there is evidence of a warm signal propagating from south to north (e.g., 4–6, 9–11, 15–17, and 26–28 October). These propagating warm signals follow wind relaxations, but are not present after every Melton et al. (2009) wind relaxation (e.g., 11 September) and sometimes occur after reductions in wind forcing that do not meet the Melton et al. (2009) relaxation criteria (e.g., 4 and 24 October). To better visualize the alongshore temperature difference, we plot the difference in the subtidal surface temperatures at the southernmost and northernmost 50 m mooring sites (ΔT, Figure 3e). Positive peaks in ΔT highlight times when surface temperatures were warmer in the south than the north. The 14 October wind relaxation event, the focus of the remaining analysis, is followed by the largest alongshore temperature gradient (black box in Figure 3).

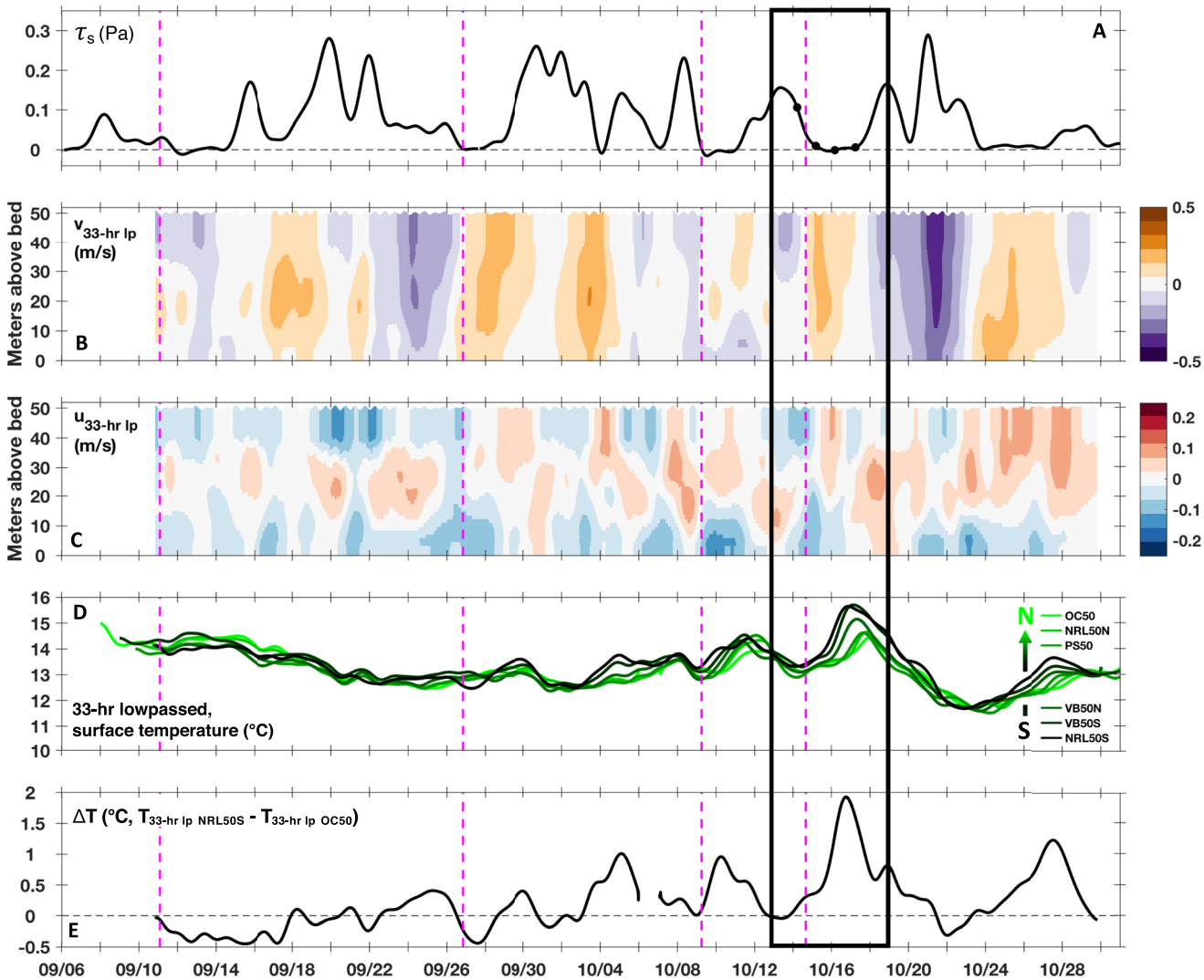

Figure 3. For the 2-month observational period: (a) 33 hr low-pass filtered wind stress rotated to the principal axis direction (Pa) from the 46011 NDBC buoy. Wind relaxation events identified by the Melton et al. (2009) criteria are noted by vertical dashed magenta lines. (b and c) 33 hr low-pass filtered northward (b) and eastward (c) velocity data from the NRL50S mooring (m s^{-1}, positive is approximately northward or onshore). (d) 33 hr low-pass filtered surface temperature data (°C) from each of the moorings on the 50 m isobath (Figure 1). (e) The difference between the subtidal surface temperatures (shown in d) at the OC50 and NRL50S moorings (°C). The black box indicates the analysis window for the October 14th relaxation event.

3.2. The October 14th Regional Wind Relaxation and Subsequent Warm Plume

3.2.1. Description of the Warm Plume

Prior to the 14 October wind relaxation event, the subtidal-frequency currents at NRL50S are predominantly directed southward (Figures 2e and 3b) and offshore at the surface, onshore at depth (Figure 3c)—a pattern consistent with classic upwelling dynamics. The water column is stratified (Figure 2c) and internal waves are a main driver of stratification and temperature variability (Figure 2d). Hours after the wind relaxation, alongshore currents become redirected northward throughout the water column (Figure 2e), a signal that persists for several days. Nearly 2 days after the wind relaxation, the surface waters warm by 3°–4°C as the buoyant plume arrives at the mooring (Figures 2c and 2f).

Daily satellite images of SST from 14 to 17 October give an aerial view of the warm water plume propagating up the coast after the regional winds relax (Figure 4). For the satellite SST data we use the 17°–18°C contours to visualize the plume boundaries, rather than the 15°C isotherm, to target the core of the plume and ignore some

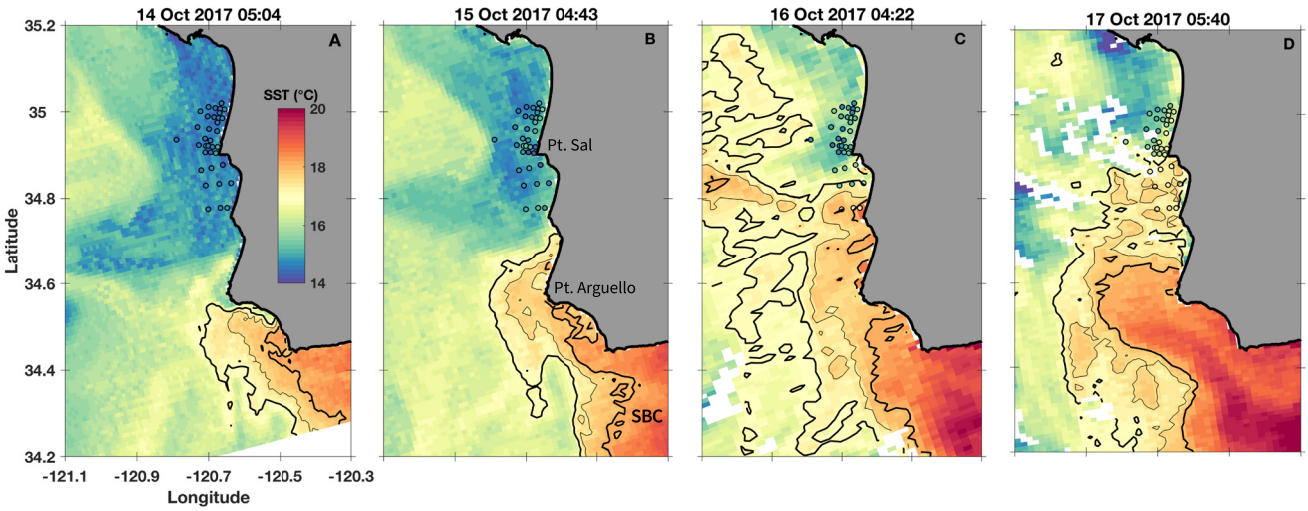

Figure 4. Approximately daily timeseries of satellite sea surface temperature (SST, details provided in Section 2.1) over the course of the October 14th regional wind relaxation event. The map area shown here is indicated in Figure 1 by the dashed black box. The 17, 17.5 (thinner line), and 18°C SST contours are shown. The surface in situ temperature data from the ISDE mooring sites are shown in the circles (same color scale). Times shown in the panels correspond to the black dots in Figure 3a.

warming signals associated with other processes. As the regional winds begin to relax (Figure 3a), surface water in the Santa Barbara Channel is 3°–4°C warmer than that outside the channel and this warm water is ejected from the channel, detaching from the coast while rounding Pt. Arguello (Figure 4a). At 15 October 04:43 UTC, approximately 13 hr after the wind relaxation, the plume has reattached to the coast and propagated past Pt. Arguello but not yet reached the ISDE mooring array (Figure 4b). Roughly 24 hr later, the plume has propagated into the ISDE region (Figure 4c) and has a wider cross-shelf extent than the mooring array. By 17 October 05:40, ∼61 hr after the relaxation, the plume has transited through about half the mooring array and reaches Pt. Sal (Figure 4d). The satellite data are corroborated by near-surface measurements of temperature from the moorings (dots in Figure 4), providing additional confidence in the observed evolution of the SST patterns associated with the propagating plume.

To provide a sense of how the warm water plume evolves as it propagates northward, we examine the 1-min unfiltered temperature data from 14 to 20 October (as in Figure 2c) for all the moorings. We use the 15°C isotherm as a proxy for the boundary of the plume for visualization, though the plume identification methods are more nuanced (Section 2.2.1) to account for the evolving nature of the plume. When the plume arrives at the southernmost mooring on the 50 m isobath, NRL50S, it is 30–40 m thick and is bottom-detached (Figure 5). The arrival is characterized by a rapid warming of the surface layer and a sharp depression of the 15°C isotherm, though some warming precedes this. A consistent feature of the plume across moorings is a relatively thin leading "nose" followed by a deepening of the thermocline that is maximal 12–48 hr after the initial plume arrival. This plume structure leads to uncertainty in the front arrival time identification process, as addressed further in Section 4.2.

The temperature data along the 50 m isobath suggests that the plume thins as it propagates north (Figure 5). To quantify the thinning, we calculate the plume thickness (h_{plume}) normalized by the total water depth (H) at each mooring site and plot it both as a map (Figure 6a) and as a function of alongshore distance (Figure 6b). The depth-normalized plume thickness shows a pattern from south to north of thinning at the deeper moorings but a relatively constant normalized thickness at the shallower moorings. The h_{plume}/H values approach 1 inshore of the 30–35 m isobaths (Figure 6c), suggesting that the offshore edge of the plume consistently intersects the bottom near that depth ($h_p \cong 30$m).

As the warm water plume transits through the array, internal waves continue to modulate conditions in the region. The internal wave influences on temperature and stratification are visible at all the moorings, but sites north of Pt. Sal appear more strongly impacted. Internal waves (seen as rapid vertical displacements of the 15°C isotherm on time scales of minutes to hours in Figure 5) had amplitudes ∼15–30 m at the northern sites compared to ∼5–10 m at the southern sites. We confirm these displacements are driven by internal tides by comparing their timing with 16 hr high-pass filtered cross-shore velocities (Figure 7). The thermocline depressions coincide with

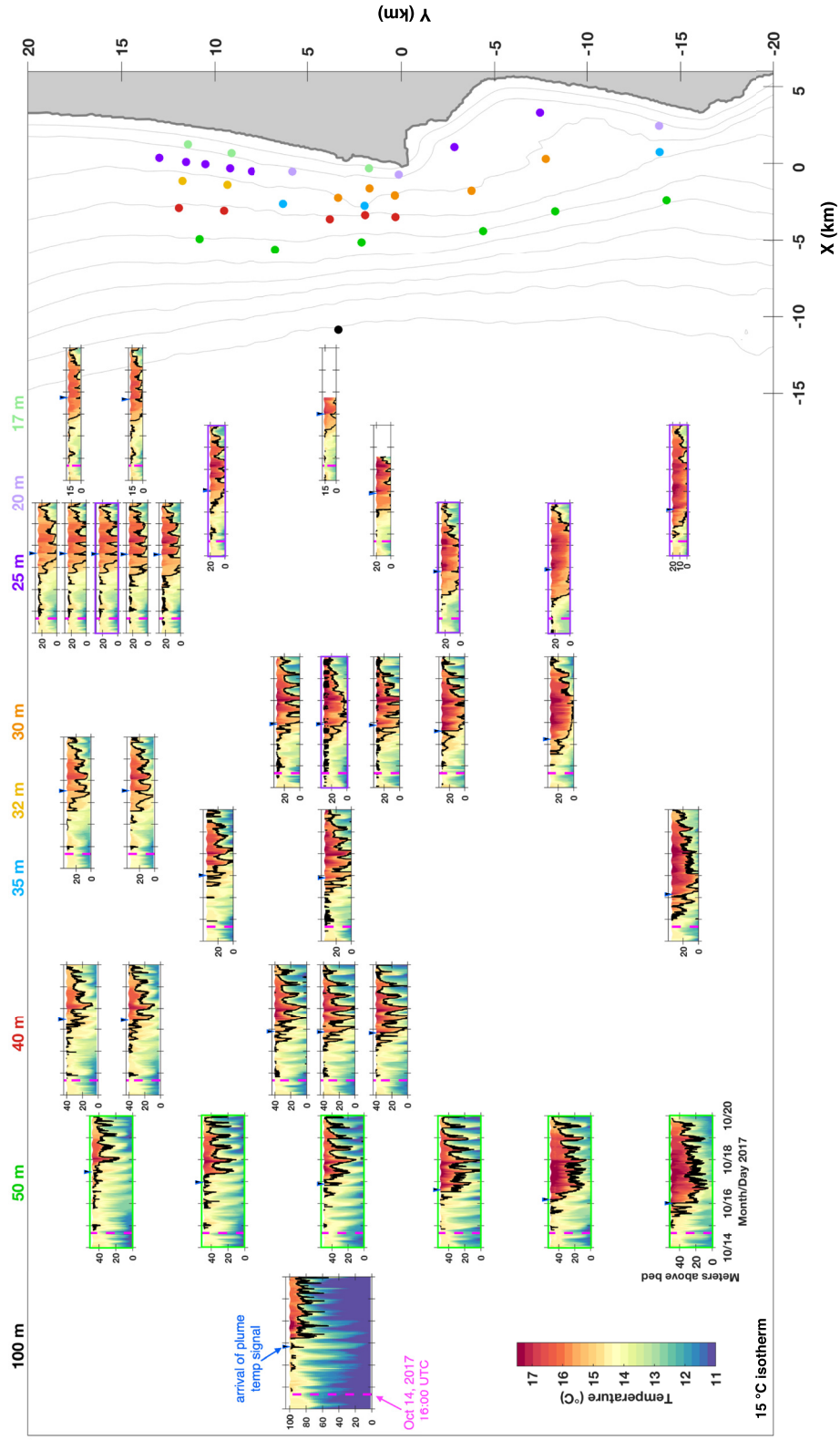

Figure 5. 1-min temperature data from 14 to 20 October 2017 for all moorings in the ISDE array. The 15°C isotherm is contoured in black. Moorings are aligned in columns by isobath, from 100 m (left) to 17 m (right), corresponding with the map on the far right. The wind relaxation time is denoted by the vertical magenta line in each timeseries plot and the arrival of the warm temperature signal (identified according to the methods in Section 2.2.1) at each mooring is indicated by the dark blue arrow at the top of each plot.

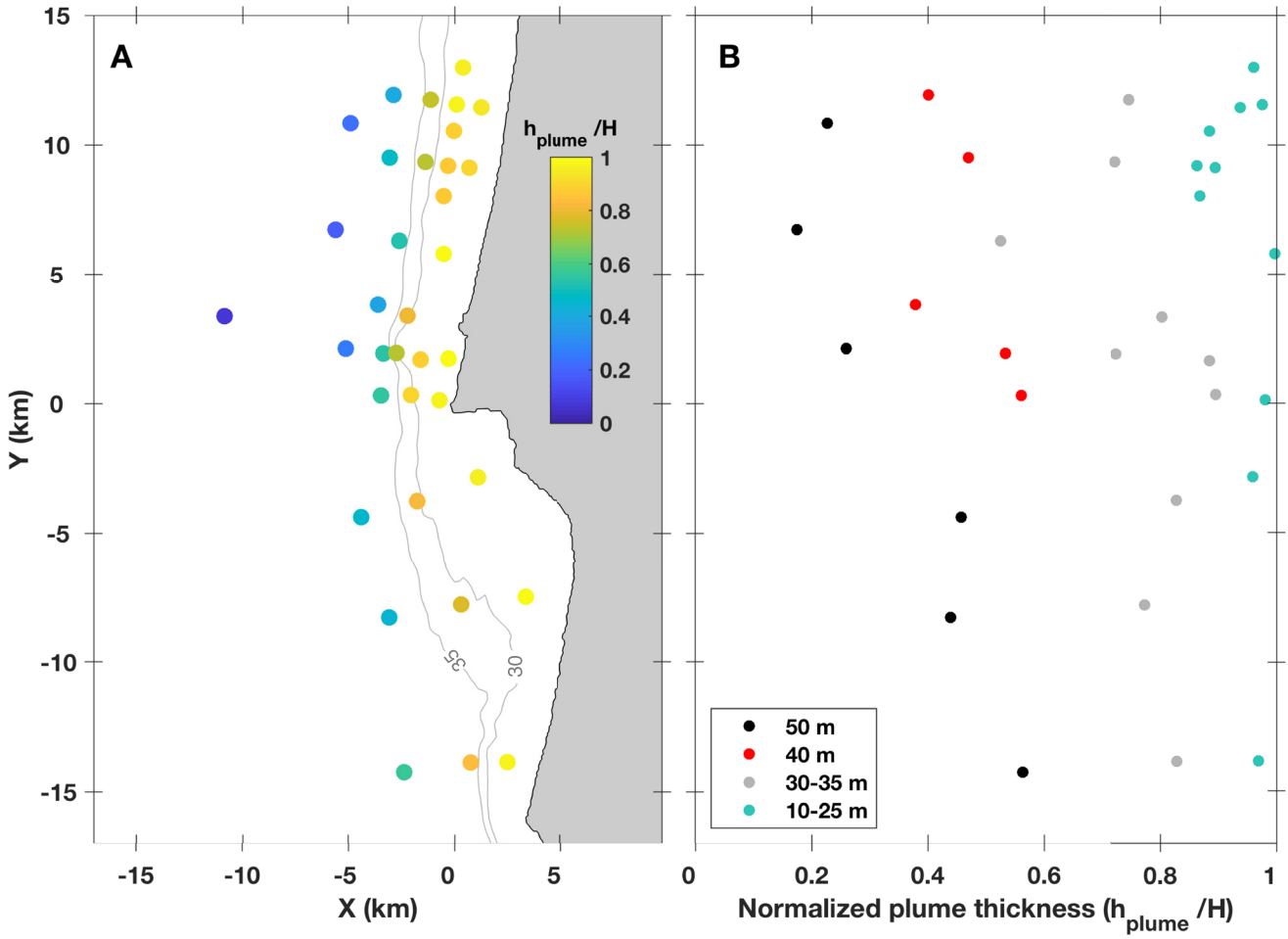

Figure 6. (a) Map of the estimated plume thickness normalized by the total water depth (h_{plume}/H) at each mooring site. The 30 and 35 m isobaths are contoured. (b) The depth-normalized plume thickness plotted as a function of alongshore distance. Dot colors indicate the depth of the mooring sites: 50 m (black), 40 m (red), 30–35 m (gray), and 10–25 m (teal).

strong onshore velocity pulses at the surface, consistent with mode-one internal waves. The internal wave velocity signals weaken inshore, but the amplitudes of the thermocline displacements are still $\sim O(10\text{m})$. The remaining analysis focuses on the plume evolution, but the potential implications of the internal wavefield are discussed in Section 4.4.

A comparison of the 1-min (Figure 5) and 33 hr low-pass filtered (Figure 8, contours) temperature data helps visualize the challenge in identifying the plume boundaries. The sharpness of the plume signal is evident in the 1-min data but can be confounded by temperature fluctuations of similar magnitude driven by internal waves. The 33 hr low-pass filtered temperature product removes the internal wave influence, isolating the plume signal more clearly but blurring the plume frontal structure. Leveraging both the 1-min and 33 hr low-pass filtered data is helpful to understanding the warm plume evolution, especially in the northern and shallow sites.

In addition to the warm plume, there is a separate, faster-propagating response to the wind relaxation. After the regional wind relaxation (Figure 8, magenta lines) and prior to the arrival of the warm plume (dark blue triangles), an alongshore northward velocity signal propagates north through the mooring array (light blue triangles). Similar to the plume temperature signal, the velocity signal is first detected at the southernmost 50 m mooring. The alongshore velocity signal is qualitatively similar at all the moorings: it is relatively depth-uniform and persists for ~4 days with some modulation by the tides. Contrary to the temperature signals that propagate through the mooring array over ~2 days (Figure 5), the velocity signal propagates the same distance in only ~10 hr.

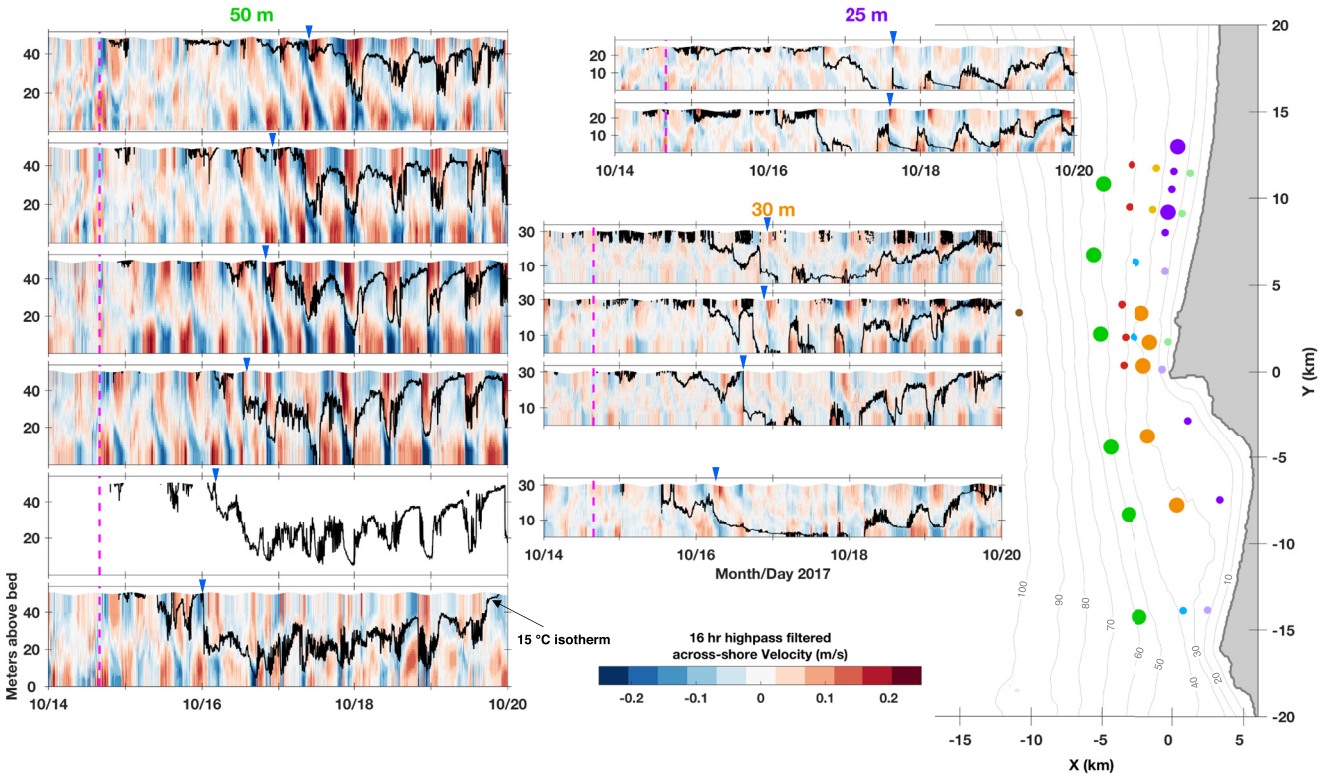

Figure 7. Mooring map of the 16 hr high-pass filtered across-shore velocities (positive shoreward) for select sites, including those along the 50 m and 25–30 m isobaths (big dots on map to the right). The 15°C isotherm from the 1-min temperature data is contoured in black. Figure configuration is otherwise the same as Figure 5.

3.2.2. A Rapidly Propagating Velocity Signal and a Slowly Propagating Temperature Signal

To visualize the different propagation speeds of the velocity and temperature signals, we plot the surface alongshore velocity and temperature data for the 50 m moorings (Figure 9). The northward propagation of both signals is clear from the sequential site arrivals, from south to north. There is a 10 hr difference between the arrival of the velocity signal at the southernmost (NRL50S) and northernmost (OC50) sites, but a 33 hr difference for the temperature signal. Given that NRL50S and OC50 are separated by ~25 km, this suggests that the alongshore velocity signal propagates at 0.7 m/s whereas the warm temperature signal associated with the buoyant plume propagates at 0.2 m/s.

Maps of the arrival times of the velocity and temperature signals demonstrate that both have a spatially nonuniform propagation speed (Figure 10). The speed of the northward velocity signal has cross-shore structure, such that the signal propagates up the coast faster nearshore than along the 50 m isobath (Figure 10a). In contrast, the speeds of the temperature signal are generally faster offshore and decrease shoreward (Figure 10b). South of Pt. Sal, the temperature front propagates inshore at a northeastward angle. This *in situ* view of the plume's propagation angle is consistent with the sequence of plume locations estimated from satellite SST (Figure 4). After the plume transits past Pt. Sal, it bends towards the coast and propagates mostly across-shore. The estimated position of the thermal plume front at hourly intervals (Figure 10b) suggests that the plume's propagation speed is nonuniform through the region, with the slowest speeds around Pt. Sal. The spatial heterogeneity in propagation speed of the temperature signal will be examined further in Section 3.2.4.

3.2.3. Temperature Reduction at the Nose of the Plume

As the plume propagates north through the mooring array, its temperature signal evolves. This is qualitatively evident in the map of 1-min temperatures (Figure 5), but we examine this more directly by looking at temperature timeseries from six pairs of offshore (50 m isobath) and onshore (20–30 m isobaths) moorings at different alongshore locations (Figure 11). Along both isobaths, the temperature difference across the plume front decreases

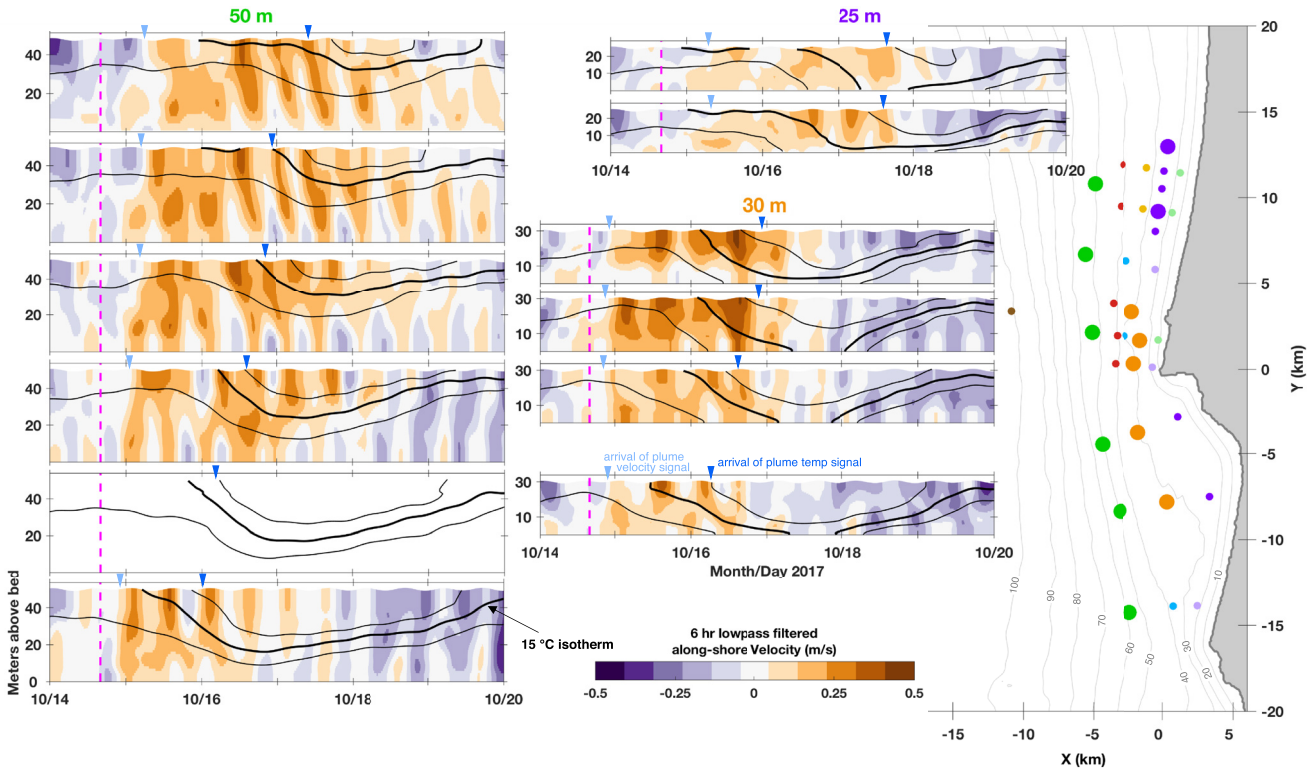

Figure 8. Mooring map of the 6 hr lowpass filtered alongshore velocities (positive is approximately northward) for select sites, including those along the 50 m and 25–30 m isobaths (big dots on map to the right). The black contour lines indicate the 14° , 15° (bold), and 16°C isotherms from the 33 hr low-pass filtered temperature. Figure configuration is otherwise the same as Figures 5 and 7.

from south (~2.5°C) to north (~1°–2°C). Because the pre-plume temperature is roughly constant, the alongshore decrease in the cross-front temperature difference is due to spatial heterogeneity of the maximum temperature in the plume. The temperature front is generally sharper at the deeper sites, and frontal sharpness generally

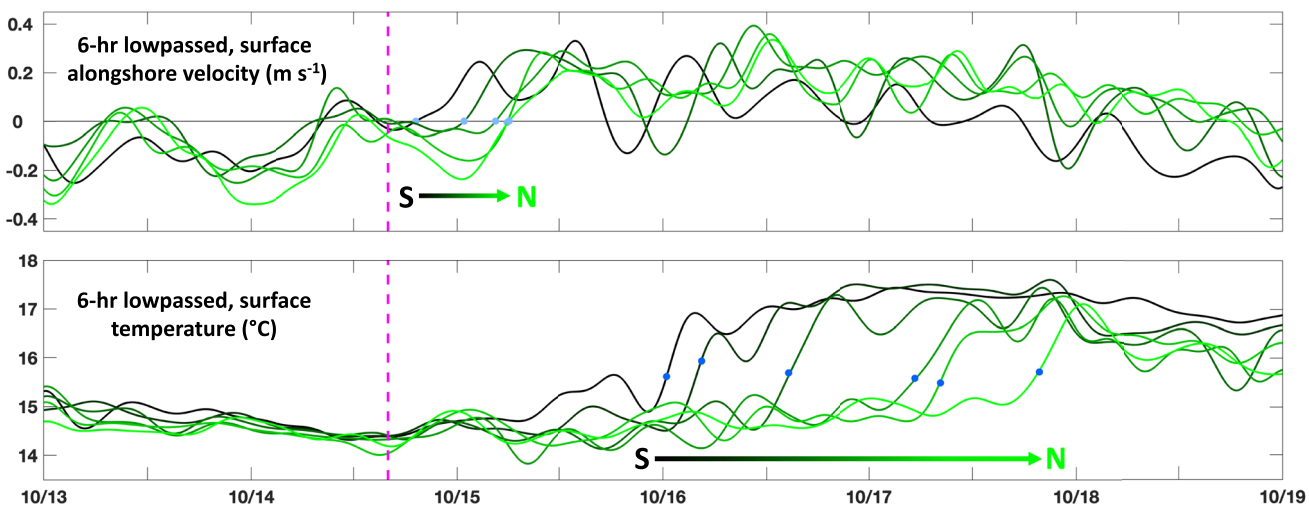

Figure 9. Timeseries of the 6 hr low-pass filtered surface alongshore velocity (top plot, m s^{-1}, positive is ~northward and 6 hr low-pass filtered surface temperature (bottom plot, °C) data for each of the 50 m moorings (Figure 1) after the October 14th relaxation event. Along-shelf distance of each site (south to north), relative to the southernmost 50 m mooring is 6.0, 10.1, 16.6, 21.3, and 25.2 km, respectively.

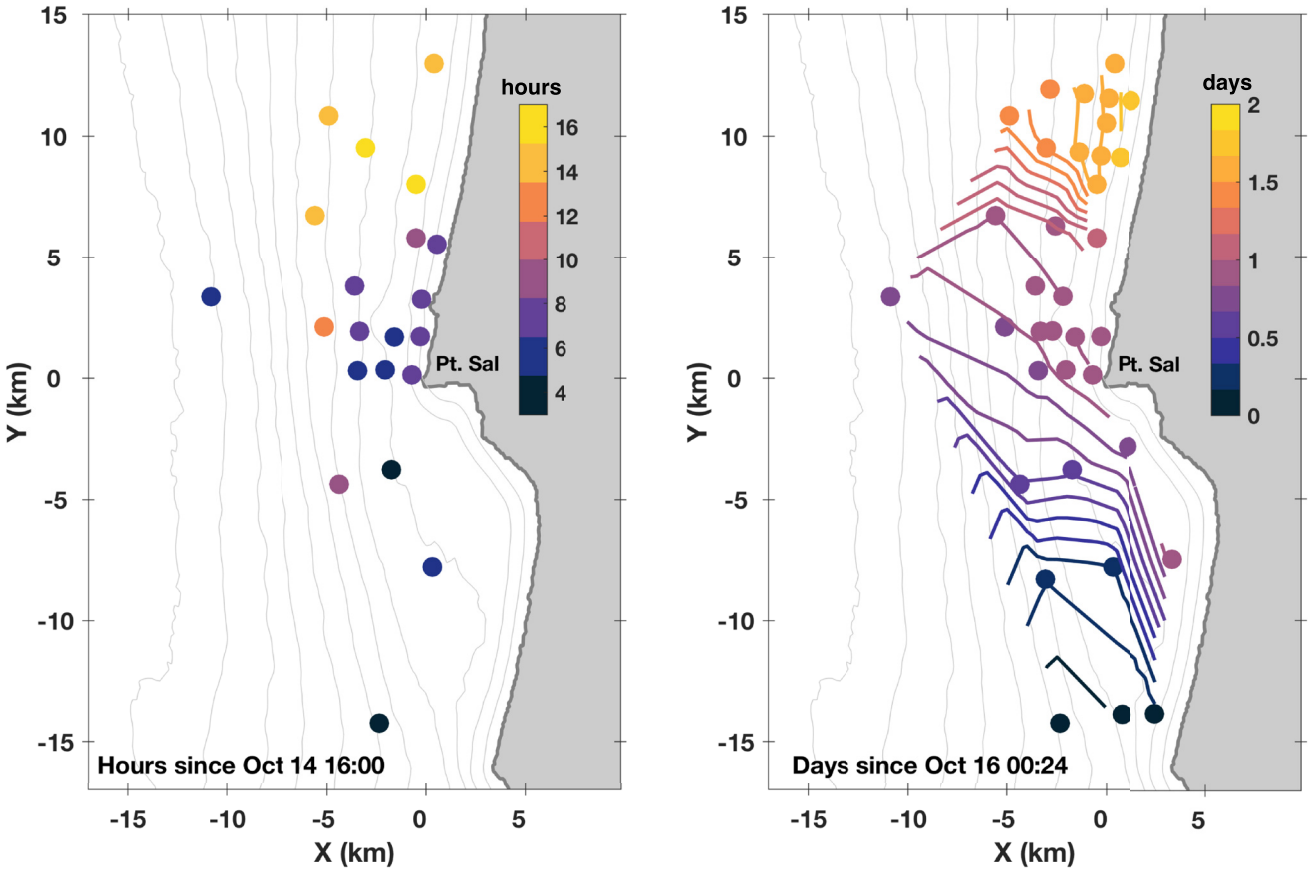

Figure 10. Arrival times of the northward velocity signal (a) and the temperature signal (b) of the warm plume after the October 14th wind relaxation event. Due to the difference in the signal propagation speeds, (a) is given in hours since 14 October 16:00 UTC and (b) is given in days since 16 October 00:24 UTC, the arrival time at NRL50S.

decreases from south to north. At the northernmost 25 m site, it takes ~3 days for the waters to reach their maximum temperature relative to the ambient conditions (compared to 36 hr at the southern site).

To quantify the alongshore reduction in plume temperature, we calculate the depth-averaged temperature within the plume at all sites after the October 14th relaxation (Figures 12a and 12b). That vertically averaged plume temperature displays a ~1.3°C decrease from south to north and a ~0.3°C decrease from offshore (50 m isobath) to inshore (~17–20 m) (Figure 12a). Plotting the same plume temperature as a function of alongshore distance, we use a linear fit to estimate that the alongshore rate of decrease in plume temperature is on average 0.04°C/km (slope of the red line in Figure 12b). We calculate the reduced gravity g' using the mean plume temperature at each site (Equation 4), demonstrating that the alongshore reduction of plume temperature corresponds with a ~0.003 m s^{-2} decrease in g' (Figure 12c). Since g' is a key factor in the theoretical propagation speed of buoyant plumes (Section 2.2.2; Lentz & Helfrich, 2002), this finding suggests that the alongshore cooling of the plume during propagation would cause a deceleration. For a constant h_p value of 30 m (Figure 6), a 0.003 m s^{-2} reduction in g' (Figure 12c) corresponds to a 0.1 m s^{-1} reduction in the theoretical plume propagation speed. In this along-shelf uniform theoretical framework, our observation of a nearly constant h_p and decreasing g' necessitates an alongshore reduction in the plume volume transport (Lentz & Helfrich, 2002).

3.2.4. Plume Frontal Propagation

To evaluate the variability of the plume frontal propagation velocity during its transit north, we map the frontal propagation speed and direction estimated from the moorings (Section 2.2.2, Figure 13a). The plume's propagation is spatiotemporally heterogeneous, with the velocity changing significantly over the 2.5 days of transit through the array. The plume first enters the array from the southwest corner, propagating northeast at ~30 cm/s.

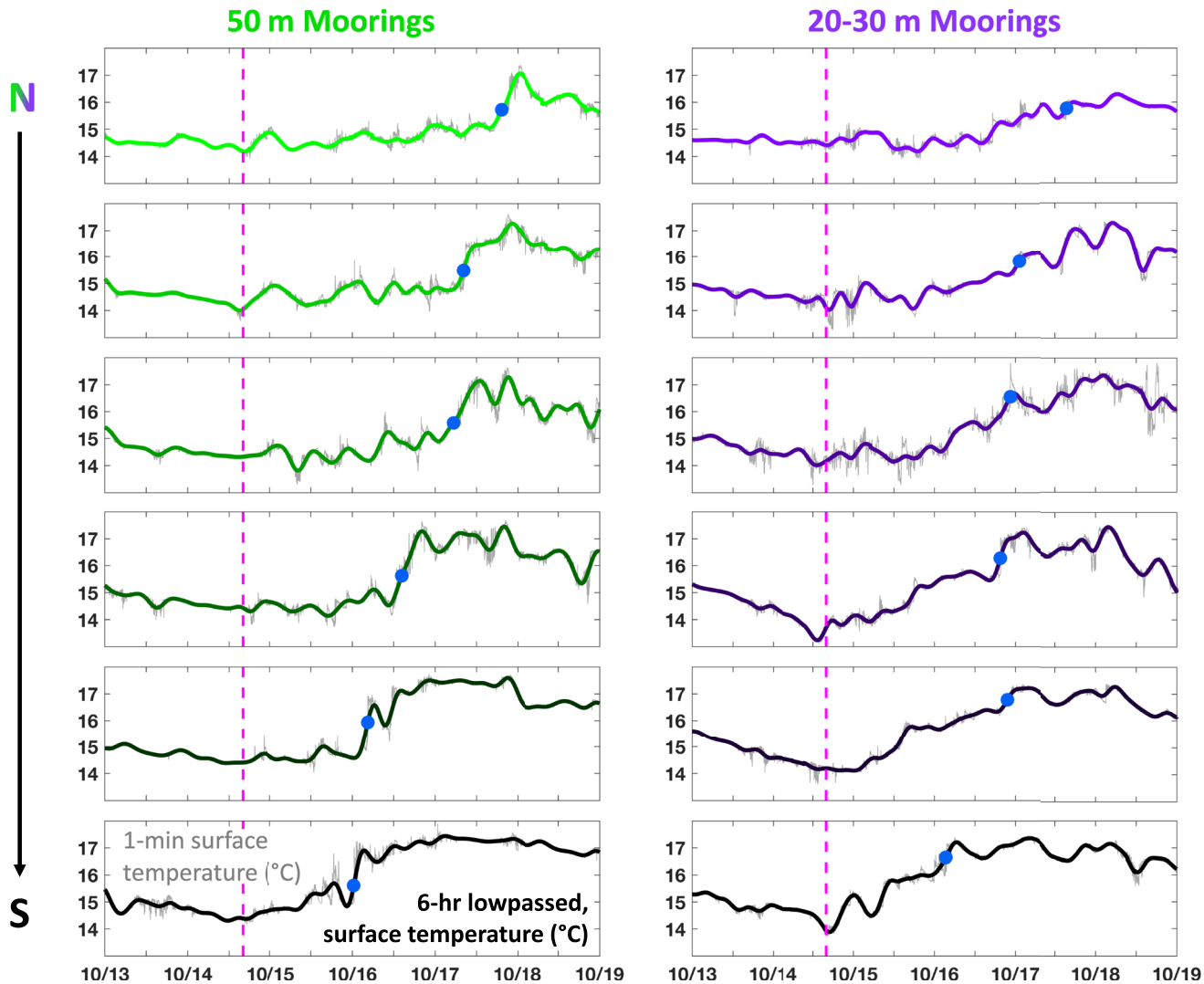

Figure 11. Timeseries of the 1-min (thin gray line) and 6 hr low-pass filtered (thick black line) surface temperature data (°C) for all the 50 m (left) and 20–30 m (right) isobath moorings (Figure 1), from north (top) to south (bottom) after the October 14, 2017 wind relaxation event (dashed pink line). The time of arrival identified for the warm plume front is indicated by the blue dot on each timeseries.

As it transits into water depths <30 m, the plume becomes directed more northward and slows to ~10–15 cm/s. Approaching Pt. Sal, the plume accelerates as it bends around the point and propagates again in the northeast direction. The plume frontal propagation is fastest just north of Pt. Sal, but then rapidly decelerates again. At the northernmost sites, the plume turns sharply eastward and no longer propagates alongshore.

The magnitude of the observed propagation velocities at sites where the plume is propagating mostly alongshore (within ±45° from northward; black arrows in Figure 13a) are compared to theoretical propagation speeds estimated from buoyant coastal plume theory (Equation 1; Lentz & Helfrich, 2002). For the theoretical estimates, speeds are computed using (a) a constant value of h_p and θ and (b) a constant h_p and alongshore variable θ (Section 2.2.2, Figure 13). We use $h_p = 30$ m, as is suggested by Figure 6. The comparison to theoretical propagation speeds highlights that the observed propagation velocity is mostly slower than predicted both south and north of Pt. Sal (~0 km in Y direction), but faster near Pt. Sal. A linear fit to the theoretical propagation speed calculated from a constant h_p and θ suggests that the alongshore reduction in g' would cause alongshore velocities to decrease at a rate of 0.3 cm s^{-1}/km alongshore. Note that this theory (Lentz & Helfrich, 2002) does not account for any background current that may advect the plume. Given that thermally buoyant plumes such as this propagate at a speed similar to the ambient currents, the ambient currents may be playing a key role here.

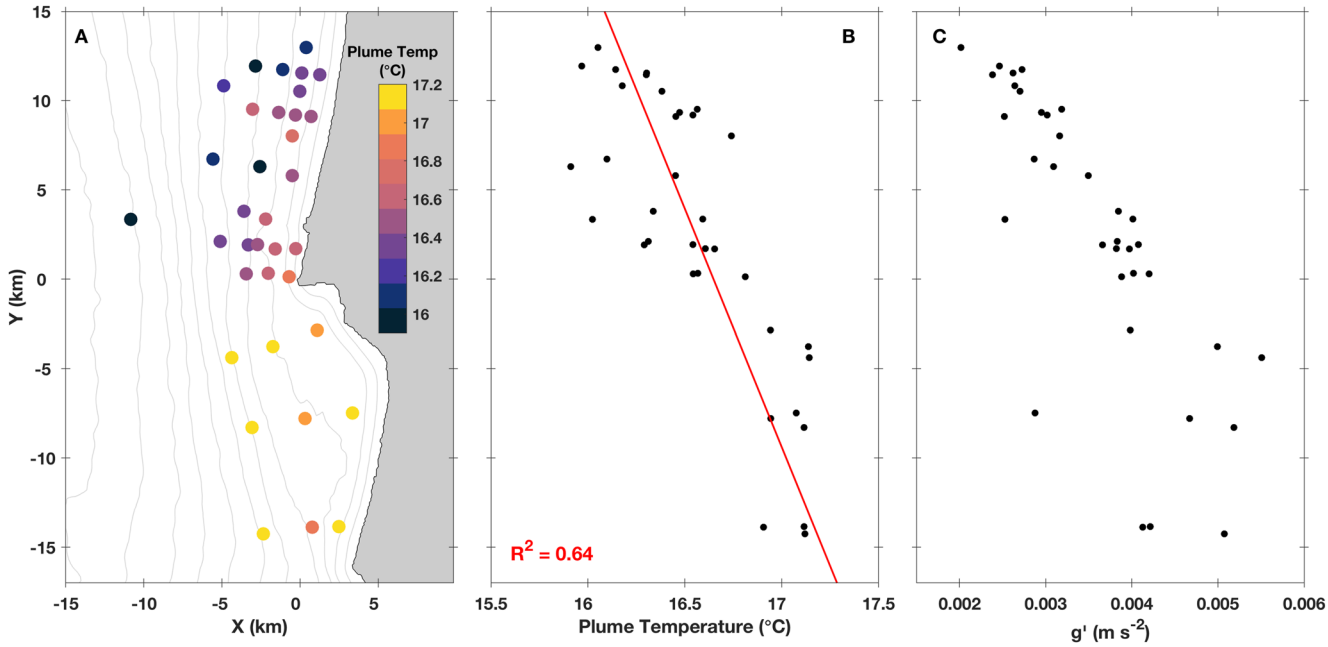

Figure 12. (a) Map of the depth-averaged temperature within the warm plume that followed the 14 October wind relaxation, as the plume passed each mooring location (note that the time differs at different locations in the plot). (b) The depth-averaged plume temperature (from a) plotted as a function of alongshore distance. (c) The reduced gravity g' of the plume as it passed each location (estimated using the mean density in the plume relative to the mean density of the ambient water ahead of the plume) plotted as a function of alongshore distance.

Compared to the observed variation in plume speed, variations in the theoretical speed estimates due to an alongshore-variable shelf slope are relatively minimal. The influence of θ variability has clear regional differences–north and south of Pt. Sal it reduces the c_p estimate (relative to that calculated from a constant θ), but near Pt Sal it increases c_p estimates (Figure 13b). The theoretical speeds should be compared to the alongshore component of the observed propagation velocities, but it is debatable how to best estimate the alongshore component here. Thus, we include both the magnitude of the observed propagation velocities (c_{obs}) and the northward component ($c_{\text{obs }y}$), which are qualitatively similar and both demonstrate an along-coast pattern that differs from that predicted by the along-shelf uniform theory (Figure 13b).

The spatial variability of the plume's propagation velocity is rather surprising given the comparatively simple spatial patterns of the plume's mean temperature (Figures 12a and 12b) and the alongshore decrease in g' (Figure 12c). Thus, to determine whether tidal advection can explain the observed spatiotemporal variations in plume frontal propagation velocity (Figure 13), we plot a sequence of maps at 2 hr intervals depicting the 33 hr low- and high-pass filtered surface currents, the surface temperature, the estimated position of the plume, and the frontal propagation velocities estimated within the 2 hr window (Figure 14). By choosing a 33 hr filter cutoff, we distinguish the subtidal frequency (low-pass filtered) currents from those driven by high-frequency processes including the barotropic and internal tide (high-pass filtered; termed "tidal currents" onwards). To minimize the direct affects of wind forcing, the 15 snapshots are taken from a 28 hr period when the wind stress is negligible. The subtidal surface currents (gray arrows) are strongest near Pt. Sal and predominantly directed northward, with a relatively weak across-shore component. Meanwhile, the tidal surface currents are spatially heterogenous and change directions over the timeseries, sometimes directed mostly across-shore and other times oriented mostly alongshore.

Comparing the timing of the tidal velocities and plume position, the patterns of frontal deceleration and acceleration appear to be unrelated to the tidal currents. For example, the plume frontal propagation would be expected to be fastest when the tidal currents align with the frontal propagation (i.e., Figures 14h–14j) and weakest when the tidal currents oppose the direction of the plume front propagation (Figures 14l–14n). However, we do not observe this. Rather we see that the tidal currents are generally directed towards the south/southwest as the plume front accelerates northward while approaching Pt Sal (Figures 14l–14m).

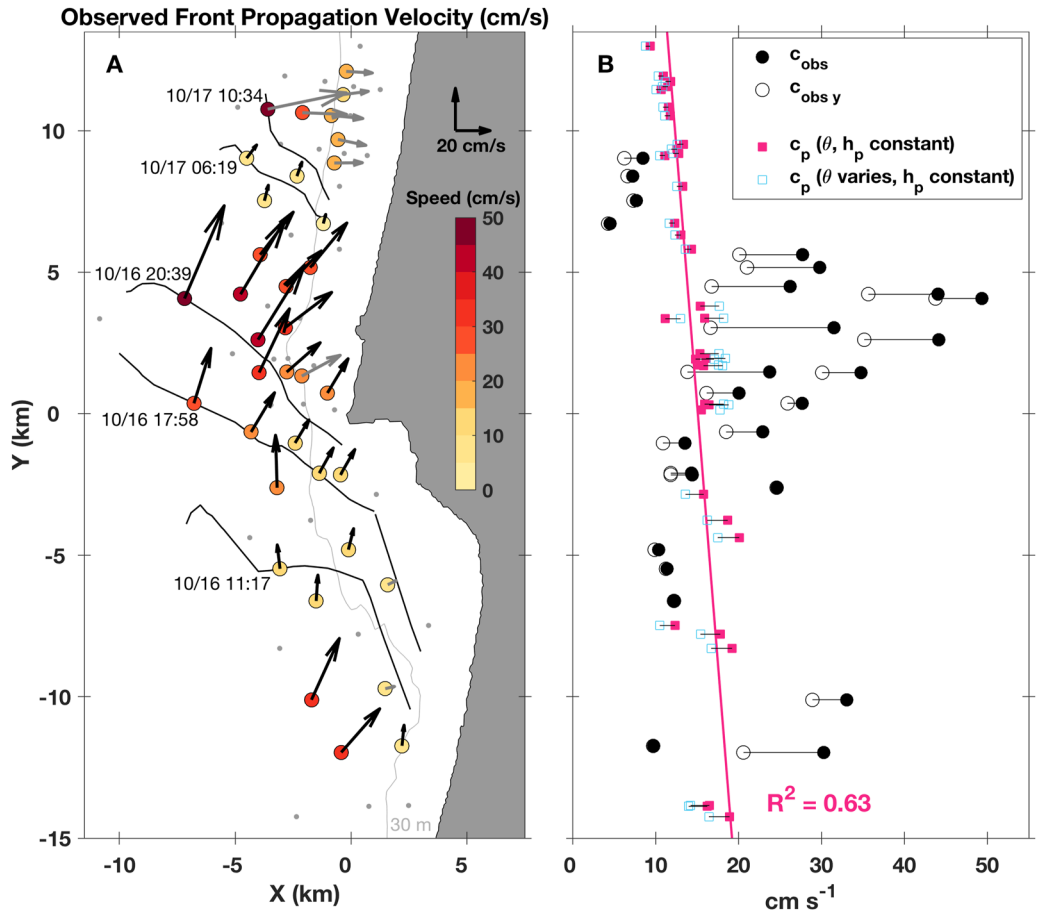

Figure 13. (a) Map of the plume propagation velocities (arrows) estimated from the arrival times at various mooring clusters (Figure 1, Section 2.2.2). The frontal propagation speed (cm s^{-1}) is shown by colored dots. Mooring sites are denoted by gray dots. Since the frontal propagation velocities are not estimated simultaneously at all mooring clusters, we include five plume front positions and the associated time of the estimation to give a sense of time progression. Arrows are black for sites where the plume propagates primarily alongshore (within ±45° of northward) and the site is included in panel (b). If the site is excluded from (b), the arrow is gray. (b) The magnitude of the observed propagation velocities (c_{obs}, black filled dots) and of the northern component of the propagation velocity ($c_{obs\ y}$, black open dots) as a function of alongshore distance. This is compared to c_p (colored squares), the theoretical propagation speed (Equation 1) based on Lentz and Helfrich (2002). Two estimates of c_p are given, calculated using: (i) a constant shelf slope (θ) and h_p (pink squares), and (ii) an alongshore variable θ but constant h_p (teal squares). The linear fit (pink line, slope = −0.3 (cm/s)/km) is for c_p calculated from case (i) only. The observations (and theoretical estimates) at each location are connected with a horizontal line for visualization purposes. Note that the locations associated with estimates of $c_{obs}/c_{obs\ y}$ and c_p are offset from each other, as the c_p values are estimated at each mooring and c_{obs} estimates are centered between mooring clusters (Figure 1).

3.3. A Comparison to Other Events

Of the plumes that followed all the regional wind relaxation events during the 2 months record, the plume after the October 14th wind relaxation had the strongest signal through the ISDE mooring array. This is visualized in Hovmöller diagrams from the six 50 m moorings, including: the 33 hr low-pass filtered surface alongshore velocity, the 6 hr low-pass filtered temperature, and the 24 hr–12 days bandpass filtered surface temperature (Figure 15). The 33 hr filter cutoff for the alongshore velocities was selected to remove the tidal variability and better visualize the signals associated with wind relaxations. The bandpass filtering of the temperature data (Figure 15d) was added to remove very low frequency modulation of the temperature and draw attention to warm features that propagate northward on timescales of days.

One important observation from the 2-month record is that the Melton et al. (2009) relaxation index does not always predict when a warm buoyant plume (as that seen by satellite SST in Figure 4) will propagate into our observational region (i.e., September 11), Since the distance of alongshore propagation of warm water plumes

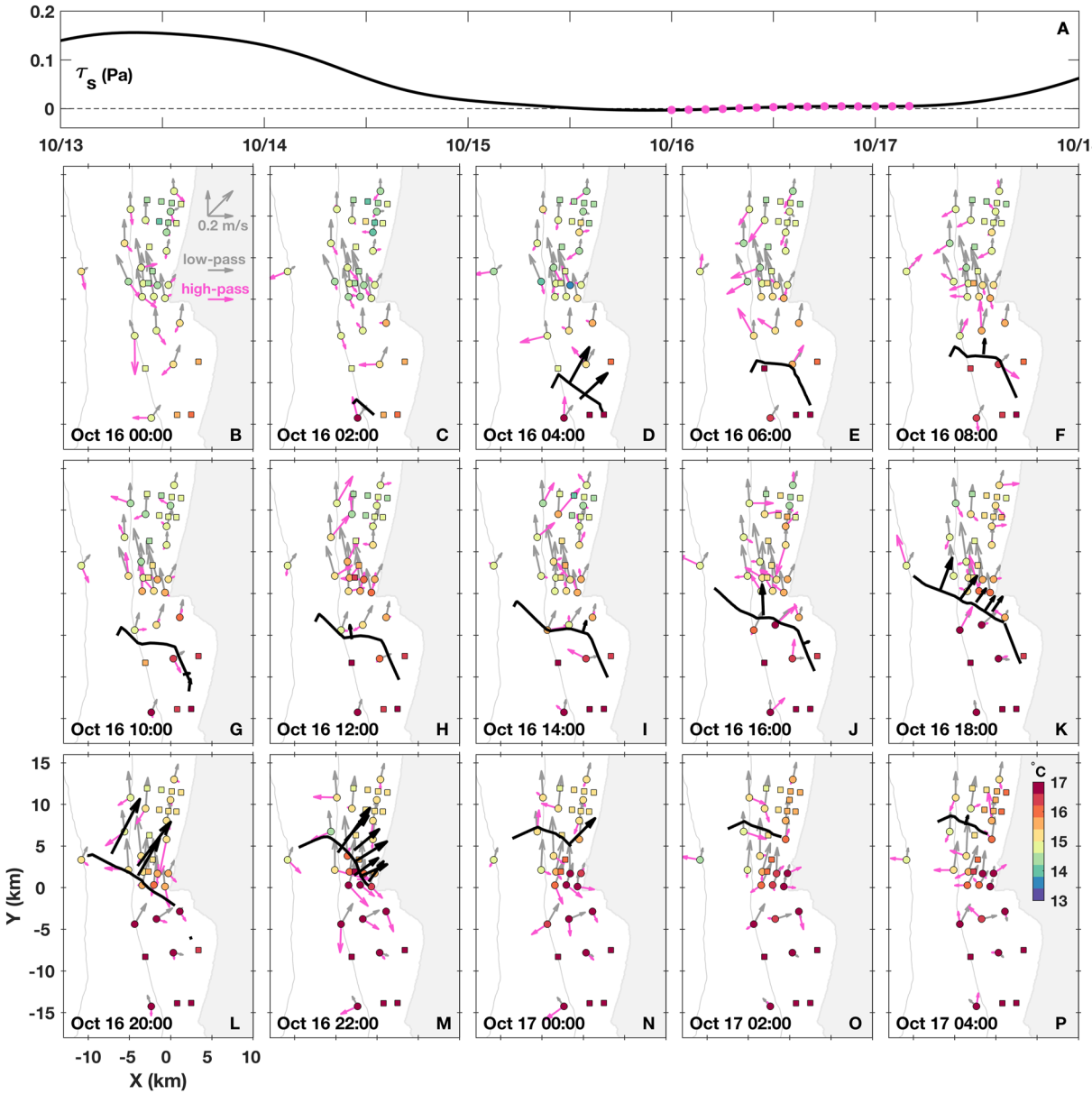

Figure 14. (a) Timeseries of the 33 hr low-pass filtered wind stress rotated to the principal axis direction from the 46011 NDBC buoy over the October 14, 2017 wind relaxation event. Pink dots show the times depicted in panels below. (b–p) Maps of the surface temperature (°C, colored circles and squares) at each mooring and the 33 hr high-pass filtered (pink arrows) and 33 hr low-pass filtered (gray arrows) surface velocities at moorings with an ADCP for 2-hr intervals from 15 October 12:00 UTC to 16 October 16:00. The location of the plume front at each time is denoted by the thick black contour and the frontal propagation velocities within ±1 hr of the noted time are shown (black arrows). Velocity data is unavailable at sites shown by squares.

depends on the conditions prior to the wind relaxation (Melton et al., 2009), there may be plumes that exit the Santa Barbara Channel but do not propagate far enough upcoast to enter the ISDE mooring array. Additionally, there are other periods of weakened wind stress that are not flagged by the Melton index as relaxations but are followed by both velocity and temperature signals that propagate through the ISDE region. For instance, the weakening wind stresses on 17 September, 4 October, and 24 October are all followed by a rapidly propagating northward velocity signal and a slower propagating warm signal. These observations suggest that the Melton et al. (2009) criteria may not capture the range of conditions that generate poleward-propagating warm plumes.

The Hovmöller diagrams (Figure 15) suggest that the October 14th event is representative of the more generalized relaxation response of this region (Washburn et al., 2011). In the 2-month record there are five other instances

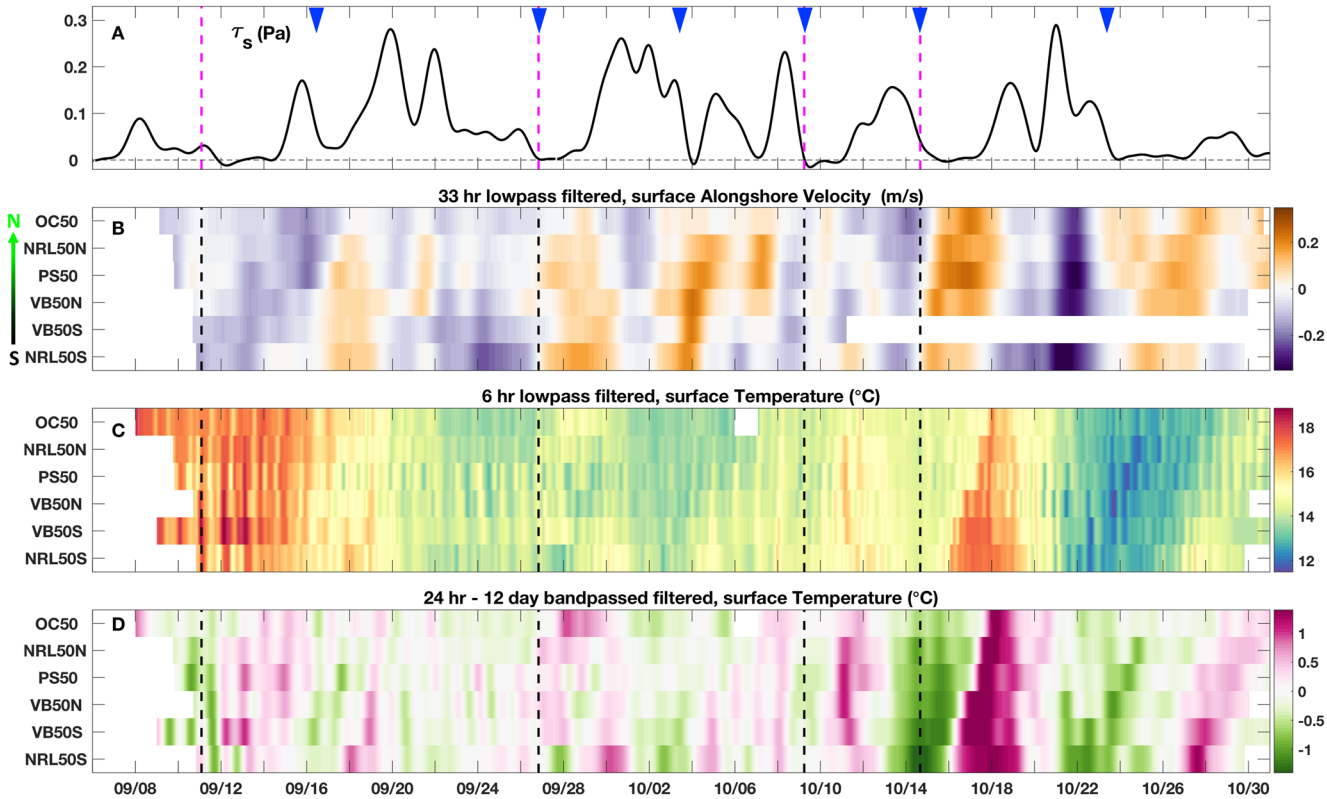

Figure 15. For the 2-month observational period, the 33 hr low-pass filtered principal axis components of wind stress (Pa) from the 46011 NDBC buoy (a), and Hovmöller diagrams of (b) 33 hr low-pass filtered, surface alongshore velocities (m s^{-1}, positive is ~northward), (c) the 6 hr low-pass filtered, surface temperature (°C), and (d) the 24 hr–12 days bandpass filtered surface (°C). Wind relaxation events identified by the Melton et al. (2009) criteria are noted by vertical dashed magenta lines. Wind relaxation events that appear to generate a northward warm plume that transits through the ISDE mooring array are indicated by blue triangles.

of a quickly propagating velocity pulse followed by a slower moving warm signal (Figure 15, blue triangles). In addition to the variable wind stress conditions, we suggest that the subtidal circulation (Figure 3) and internal wave conditions (Figure 2; McSweeney, Lerczak, Barth, Becherer, Colosi, et al., 2020) conditions play a role in determining how far north the plume signal propagates and whether the plume signal can be easily distinguished from signals driven by other shelf processes.

4. Discussion

4.1. The 2-Part Ocean Response to a Wind Relaxation: A Comparison to Previous Studies

The detailed characterization of a dual oceanic response to a regional wind relaxation event – that is, the rapid propagation of a poleward current signal and the slower propagation of a warm plume - is a main result from this work. This 2-part response is consistent with observations of the oceanic response to wind relaxations averaged over many relaxation events (Melton et al., 2009; Washburn et al., 2011). In contrast to previous work however, our analysis primarily focuses on a single event and leverages a data set that is highly resolved spatially to provide insight about the heterogeneity of these two signals and their evolution while propagating alongshore.

For the velocity signal that propagates ahead of the buoyant plume, we first confirm similarities to previous observations by Melton et al. (2009): (a) that the velocity signal extends the full water column depth, (b) that the poleward current arrives ~O(1 day) ahead of the warm water, and (c) that the northward current intensifies a few hours ahead of the warm plume arrival (Figures 8 and 14). Our data further reveals that the poleward velocity signal propagates north past Pt. Sal (beyond the scope of the previous PISCO observations) and spans across the shelf from the 17 m isobath to the 100 m isobath (offshore of the PISCO data). The rapid velocity response following the wind relaxation has a spatially heterogenous propagation speed (Figure 10a), with an average value of ~0.7 m s^{-1}.

These observations are consistent with previous suggestions that the poleward velocity signal is caused by an alongshore pressure gradient that is normally balanced by the upwelling-favorable wind stress and becomes unbalanced when the wind relaxes (Cudaback et al., 2005; Harms & Winant, 1998; Melton et al., 2009; Send et al., 1987; Washburn et al., 2011). Poleward counter-currents have similarly been studied along the Oregon coast (Gan & Allen, 2002), the Gulf of Cádiz (García-Lafuente et al., 2006; Júnior et al., 2021; Relvas & Barton, 2002), the southern Benguela coast (Fawcett et al., 2008), and northern California (Woodson et al., 2009). Other studies have used an alongshore momentum balance analysis to demonstrate the role of the along-shelf pressure gradient change in driving these poleward currents (Júnior et al., 2021; Lentz et al., 2003; Relvas & Barton, 2002).

Our observations similarly expand on existing knowledge of thermally buoyant propagating plumes. Specifically, the data provide new insight about how a warm plume evolves heterogeneously in space and time, becoming thinner (Figure 6), cooler (Figure 12), and more influenced by internal waves (Figure 7) as it transits north. Though the plume is predicted by along-shelf uniform theory to monotonically decelerate due to the alongshore reduction of g', we do not observe that. Rather, the plume velocity is very nonuniform, with decelerations and accelerations that are unexplained by the alongshore reduction of g' or advection by tidal currents (Figure 13). Possible causes of these nonuniformities in frontal propagation velocity include spatially heterogenous bottom friction, headland influences, and other non-local influences such as a larger-scale pressure gradient developing. Our analysis does not clarify the dynamics modulating frontal propagation velocity enough to predict the nonuniform behavior of a given plume, but it does demonstrate the complexity of a plume front's velocity and illustrate that a plume can be more variable than a single speed estimate suggests.

Previous studies of plumes in this region provide valuable information to contextualize our observations of the October 14, 2017 plume event. For example, the alongshore reduction in g' calculated from the average temperature within the plume (Figure 12c) is qualitatively consistent with a modeling study of a plume in the same region (Suanda et al., 2016) but exhibits a slightly larger range of g' values: 2–5.5 $\times$ 10^{-3} m s^{-2} compared to 2.5–3.5 $\times$ 10^{-3} m s^{-2}. This suggests a greater alongshore evolution in the October 14, 2017 event than the plume case discussed in Suanda et al. (2016). We also observe that the 30–35 m isobath roughly distinguishes the onshore (bottom-attached) and offshore (bottom-detached) regions of the plume (Figure 5) — a finding consistent with regional plume modeling (Suanda et al., 2016).

The plume dynamics can be related to a theoretical framework (Lentz & Helfrich, 2002), where the ratio c_w/c_α determines the importance of bottom friction and whether the plume will be surface-trapped (c_w/c_α <<1) or slope-controlled (c_w/c_α >> 1). In a previous observational study of 39 plume events in this region, c_w/c_α ranged from 0.48 to 75 with a median value of 1.7 (Washburn et al., 2011), suggesting that most plumes were slope-controlled. In our analysis of a single event, the estimates of c_w/c_α across the region range from 0.6 to 1.3, with a median of 0.89 and an average of 0.88. These estimates suggest that our observations represent a plume that truly sits in intermediate parameter space, possibly more so than some of the plumes described by Washburn et al. (2011).

4.2. Uncertainty in the Plume Arrival Identification and Frontal Propagation Speeds

Given how the plume's temperature signal evolves, the plume arrival time is more uncertain in the northern and shallower sites. We use the identification methods detailed in Section 2.2.1. for consistency across all mooring sites, but it is unclear whether the arrival times (blue triangles in Figures 5, 7 and 8; blue dots in Figures 9 and 11) are always the best representation of the plume front. This issue is further complicated by the fact that internal waves can generate temperature fluctuations of similar magnitudes within the same timeframe as a plume transits past a mooring (Figure 7). Though internal waves influence the whole region (Figures 5 and 7), it is more challenging to distinguish the plume signal from the internal wave signal in the northern inshore region, as the plume's temperature front becomes smaller in magnitude and less sharp (Figure 11).

Given the increased uncertainty in plume identification in the northern and shallow sites, uncertainty in the frontal propagation velocity analysis also needs to be considered. A sensitivity analysis of various frontal identification methods yielded consistent spatiotemporal patterns in propagation velocity. The quantitative details were sensitive to the identification method used, but the patterns of where/when the propagation velocities are strongest did not change.

4.3. Interpreting Propagation Speeds

The elucidation of the spatiotemporal heterogeneity of a plume front's propagation velocity is, to our knowledge, a novel contribution of this work. Previous observations have captured plumes with spatially variable frontal propagation speeds, such as data from the Hudson River plume (a freshwater outflow plume) that demonstrated an along-coast deceleration due to a diminishing g' (Jurisa & Chant, 2012). However, other studies have been limited in their ability to resolve the finer details of how frontal propagation speed can change. Based on the fact that the surface tidal currents cannot explain the acceleration of the plume around Pt. Sal (Figure 13a), we suggest that the observed nonuniformity of the plume front velocity may be caused by bottom friction heterogeneity or headland influences. Other studies have demonstrated that wind conditions can influence a plume's propagation or frontal advection (Jurisa & Chant, 2012, 2013; Lentz & Largier, 2006; Woodson et al., 2009). In our case, the wind stress picks back up on 17 October after the plume front acceleration (Figure 14).

Beyond the detailed analysis of the 14 October event, this work additionally demonstrates event-to-event variability in the average plume propagation speed. From the 6 plume events observed in the 2 months record, a range of propagation speeds is evident from the different slopes of elevated temperature signals in the Hovmöller diagram (Figure 15d). The plume we analyzed appears to be mid-range in terms of propagation speed, which parallels the modeling analysis of Suanda et al. (2016) that targeted a model case (their Figure 11) mid-range of speeds estimated by Washburn et al. (2011).

4.4. Interactions Between the Thermal Plume and Internal Waves

Perhaps one of the most novel aspects of this analysis is the insight it offers about the overlapping and possibly interacting ways in which buoyant plumes and internal waves influence the same region on similar spatial and time scales. Though it is well known that the inner shelf is a dynamically complex region, much of our present understanding of the inner shelf is rooted in analyses focused on singular processes. Previously, local studies about internal waves (Colosi et al., 2018; Kumar et al., 2019; McSweeney, Lerczak, Barth, Becherer, Colosi, et al., 2020; McSweeney, Lerczak, Barth, Becherer, MacKinnon, et al., 2020) and buoyant plumes (Melton et al., 2009; Suanda et al., 2016; Washburn et al., 2011) have largely been conducted without considering the joint influences of these two processes along the central California coast. This analysis hints at the importance of their overlap in several ways. First, it suggests that variability driven by internal waves can obscure the signals from buoyant plumes (and vice versa), challenging identification efforts. In our analysis, the influences of internal waves significantly contributed to uncertainty in plume identification both in the shallow and northern sites (Figure 11). Despite trying various identification techniques (Section 5.2), we found it difficult to develop a robust approach to separate the temperature signals associated with the internal waves and the buoyant plume. Second, the analysis suggests that the relative contribution of internal waves and buoyant thermal plumes to inner shelf temperature and stratification variability can be difficult to quantify (Figures 2, 5 and 11).

Visualizations of the plume (Figures 5 and 8) and the internal tidal currents (Figure 7) also raise an important question: Do cross-shore propagating internal waves contribute substantially to mixing (and destruction?) of the alongshore-propagating plume? We do not explore that question directly, but note the presence of multiple internal waves per day during the period the plume transits through the region. Given how strongly the internal waves affect stratification (Figures 2 and 7; McSweeney, Lerczak, Barth, Becherer, Colosi, et al., 2020; McSweeney, Lerczak, Barth, Becherer, MacKinnon, et al., 2020) and mixing (Becherer et al., 2020; Lamb, 2014), our observations suggest that the internal waves themselves may be contributing to the diminishing signals of the plume (reduced temperature gradient, thinning depth, and less sharp front) as it transited through the mooring array.

5. Summary

We present observations from 35 moorings centered off Pt. Sal, CA that capture the oceanic response to a regional wind relaxation event that occurred on October 14, 2017. After the predominantly upwelling favorable winds relaxed, warm water from the Santa Barbara Channel transited up the coast as a buoyant plume, causing temperature and stratification variability as it moved north. A 4-day timeseries of sea surface temperature data from the AVHRR MetOp-B satellite provides a sense of the spatial extent of the warm plume as it propagated north and corroborates the timing of the plume arrival at the mooring array. The satellite data also confirms that the plume width exceeds the cross-shore width of the mooring array. The *in situ* mooring data capture both regions where

the plume was bottom-attached and detached, resolving the cross-shore structure of the plume and its evolution during propagation.

Two distinct, northward-propagating signals are observed in the mooring data after the wind relaxation: (a) an alongshore velocity signal propagating at ∼0.7 m/s and (b) a warm buoyant plume front propagating at ∼0.2 m/s. The velocity signal extends through the whole water column and transits quickly through the array. The warm temperature signal has more spatial complexity, with details that evolve in the 34 hr it takes to propagate 25 km alongshore. The plume thickness decreases as it propagates, and the plume becomes bottom detached around the 30–35 m isobath.

An analysis of the vertically averaged temperature within the plume reveals that the plume cools at an average rate of ∼0.04°C/km during propagation, yielding a 0.003 m s^{-2} alongshore reduction in g' over the observational region. The plume signal becomes difficult to identify in the northern and shallower sites, where temperature fluctuations associated with the plume arrival are of comparable magnitude to temperature fluctuations driven by internal waves. Contributing to the challenge of identifying the plume at these sites, the warming signal is also more gradual in this mooring data. Despite the uncertainty in the plume front arrival times, we show robustly that a warm anomaly associated with the buoyant plume transits through the entire mooring array and that this warm signal decreases in magnitude from south to north.

Using the arrival times of the warm plume at each mooring, we estimate the propagation velocity of the plume as it transits through the array. From a map of the time-varying frontal position, it is evident that the plume front velocity is highly nonuniform. Based on a series of 2-hr-interval maps that include the surface subtidal and tidal currents as well as the plume front position, we conclude that tidal advection does not explain the plume accelerations. We suggest that heterogeneity of the plume's propagation velocity could be due to the development of a large-scale pressure gradient, headland influences, or nonuniform bottom friction.

The analysis mostly focuses on a detailed investigation of the plume evolution after the October 14, 2017 wind relaxation event, but we also observed five other wind relaxations that produced similar propagating alongshore velocity and warm signals over the 2-month period. The high spatial resolution of the observations provide new insight about how these two oceanic responses differ in their propagation speed and spatial structure, as well as demonstrate that buoyant plumes originating from Santa Barbara Channel persist further north than has previously been observed (Melton et al., 2009; Washburn et al., 2011). Due to its thermal (rather than fresh) nature, the plume discussed in this analysis has a smaller g' than many buoyant plumes that have been studied previously. However, the plume dynamics we describe are consistent with broader buoyant plume theory and observations from fresh water plumes.

Our analysis suggests that competing oceanic processes, such as internal waves and headland flows, may affect the evolution of a buoyant plume as it propagates north. We suggest that internal waves in particular may contribute to plume mixing and cooling, thus influencing the destruction of a poleward propagating thermal plume. This study highlights that buoyant plumes contribute to temperature and stratification variability across the inner shelf on spatiotemporal scales (hours to days; ∼1–10 km) of comparable magnitude to variability driven by other inner shelf processes. Detangling the influences and interactions of these processes is fundamental to better understanding the factors that modulate inner shelf conditions.

Data Availability Statement

The ISDE mooring data are available at https://doi.org/10.6075/J0WD3Z3Q.

References

Aristizábal, M. F., Fewings, M. R., & Washburn, L. (2017). Effects of the relaxation of upwelling-favorable winds on the diurnal and semidiurnal water temperature fluctuations in the Santa Barbara Channel, California. *Journal of Geophysical Research: Oceans*, *122*, 7958–7977. https://doi.org/10.1002/2017JC013199

Becherer, J., Moum, J. N., Colosi, J. A., Lerczak, J. A., & McSweeney, J. M. (2020). Turbulence asymmetries in bottom boundary layer velocity pulses associated with onshore-propagating nonlinear internal waves. *Journal of Physical Oceanography*, *50*, 2373–2391. https://doi.org/10.1175/JPO-D-19-0178.1

Chapman, D. C., & Lentz, S. J. (1994). Trapping of a coastal density front by the bottom boundary layer. *Journal of Physical Oceanography*, *24*, 1464–1479. https://doi.org/10.1175/1520-0485(1994)024<1464:toacdf>2.0.co;2

Acknowledgments
This study is dedicated to our beloved friend, Nirnimesh Kumar, who shared an enthusiasm for detangling complex processes and with whom we enjoyed conversations about this project. Many individuals were involved in data collection and processing, and the authors thank everyone who contributed to the data set. The authors also thank Phil Barbour for processing the wind data and Chris Gotschalk for providing the Melton et al. (2009) wind relaxation indices. The authors are grateful to Libe Washburn, Ata Suanda, and Maria Aristizábal for providing feedback and sharing code. Finally, the authors express gratitude to two anonymous reviewers for suggestions that greatly improved the manuscript. Support for this project came from ONR grant N00014-15-1-2617, NSF Physical Oceanography Award 1949067, and the NASA Ocean Vector Winds Science Team grant 80NSSC18K1611.

Colosi, J. A., Kumar, N., Suanda, S. H., Freismuth, T. M., & MacMahan, J. H. (2018). Statistics of internal tide bores and internal solitary waves observed on the inner continental shelf off Point Sal, California. *Journal of Physical Oceanography*, *48*, 123–143. https://doi.org/10.1175/JPO-D-17-0045.1

Cudaback, C. N., Washburn, L., & Dever, E. (2005). Subtidal inner-shelf circulation near Point Conception, California. *Journal of Geophysical Research*, *110*. https://doi.org/10.1029/2004jc002608

Dorman, C. E., & Winant, C. D. (2000). The structure and variability of the marine atmosphere around the Santa Barbara Channel. *Monthly Weather Review*, *128*, 261–282. https://doi.org/10.1175/1520-0493(2000)128<0261:tsavot>2.0.co;2

Dudas, S. E., Grantham, B. A., Kirincich, A. R., Menge, B. A., Lubchenco, J., & Barth, J. A. (2009). Current reversals as determinants of intertidal recruitment on the central Oregon coast. *ICES Journal of Marine Science*, *66*, 396–407. https://doi.org/10.1093/icesjms/fsn179

Edson, J. B., Jampana, V., Weller, R. A., Bigorre, S. P., Plueddemann, A. J., Fairall, C. W., et al. (2013). On the exchange of momentum over the open ocean. *Journal of Physical Oceanography*, *43*, 1589–1610. https://doi.org/10.1175/jpo-d-12-0173.1

EUMETSAT. (2020). *METOP_B AVHRR swath SST data set. Version 1*. PO.DAAC. CA, USA. https://doi.org/10.5067/GHAMB-2PO02

Fawcett, A. L., Pitcher, G. C., & Shillington, F. A. (2008). Nearshore currents on the southern Namaqua shelf of the Benguela upwelling system. *Continental Shelf Research*, *28*, 1026–1039. https://doi.org/10.1016/j.csr.2008.02.005

Feddersen, F., MacMahan, J. H., Freismuth, T. M., Gough, M. K., & Kovatch, M. (2020). Inner-shelf vertical and alongshore temperature variability in the subtidal, diurnal, and semidiurnal bands along the central California coastline with headlands. *Journal of Geophysical Research: Oceans*, *125*, e2019JC015347. https://doi.org/10.1029/2019JC015347

Fewings, M. R., Washburn, L., Dorman, C. E., Gotschalk, C., & Lombardo, K. (2016). Synoptic forcing of wind relaxations at Pt. Conception, California. *Journal of Geophysical Research: Oceans*, *121*, 5711–5730. https://doi.org/10.1002/2016jc011699

Fewings, M. R., Washburn, L., & Ohlmann, J. C. (2015). Coastal water circulation patterns around the northern Channel Islands and Point Conception, California. *Progress in Oceanography*, *138*, 283–304. https://doi.org/10.1016/j.pocean.2015.10.001

Gan, J., & Allen, J. S. (2002). A modeling study of shelf circulation off northern California in the region of the Coastal Ocean Dynamics Experiment: Response to relaxation of upwelling winds. *Journal of Geophysical Research*, *107*, 1–6. https://doi.org/10.1029/2000jc000768

García-Lafuente, J., Delgado, J., Criado-Aldeanueva, F., Bruno, M., del Río, J., & Vargas, J. M. (2006). Water mass circulation on the continental shelf of the Gulf of Cádiz. *Deep Sea Research Part II: Topical Studies in Oceanography*, *53*, 1182–1197.

Garel, E., Laiz, I., Drago, T., & Relvas, P. (2016). Characterisation of coastal counter-currents on the inner shelf of the Gulf of Cadiz. *Journal of Marine Systems*, *155*, 19–34. https://doi.org/10.1016/j.jmarsys.2015.11.001

Garwood, J. C., Lucas, A. J., Naughton, P., Alford, M. H., Roberts, P. L. D., Jaffe, J. S., et al. (2020). A novel cross-shore transport mechanism revealed by subsurface, robotic larval mimics: Internal wave deformation of the background velocity field. *Limnology and Oceanography*, *65*, 1456–1470.

Harms, S., & Winant, C. D. (1998). Characteristic patterns of the circulation in the Santa Barbara Channel. *Journal of Geophysical Research*, *103*, 3041–3065. https://doi.org/10.1029/97jc02393

Hendershott, M. C., & Winant, C. D. (1996). Surface circulation in the Santa Barbara channel. *Oceanography*, *9*, 114–121. https://doi.org/10.5670/oceanog.1996.14

Júnior, L. D. O., Garel, E., & Relvas, P. (2021). The structure of incipient coastal counter currents in South Portugal as indicator of their forcing agents. *Journal of Marine Systems*, *214*, 103486.

Jurisa, J. T., & Chant, R. (2012). The coupled Hudson River estuarine-plume response to variable wind and river forcings. *Ocean Dynamics*, *62*, 771–784. https://doi.org/10.1007/s10236-012-0527-7

Jurisa, J. T., & Chant, R. J. (2013). Impact of offshore winds on a buoyant river plume system. *Journal of Physical Oceanography*, *43*, 2571–2587. https://doi.org/10.1175/jpo-d-12-0118.1

Kersalé, M., Marie, L., Le Cann, B., Serpette, A., Lathuilière, C., Le Boyer, A., et al. (2016). Poleward along-shore current pulses on the inner shelf of the Bay of Biscay. *Estuarine, Coastal and Shelf Science*, *179*, 155–171.

Kosro, P. M. (1987). Structure of the coastal current field off northern California during the Coastal Ocean Dynamics Experiment. *Journal of Geophysical Research: Oceans*, *92*, 1637–1654. https://doi.org/10.1029/jc092ic02p01637

Kumar, N., Lerczak, J. A., Xu, T., Waterhouse, A. F., Thomson, J., Terrill, E. J., et al. (2021). The inner-shelf dynamics experiment. *Bulletin of the American Meteorological Society*, *102*, 1–77. https://doi.org/10.1175/BAMS-D-19-0281.1

Kumar, N., Suanda, S. H., Colosi, J. A., Haas, K., Di Lorenzo, E., Miller, A. J., & Edwards, C. A. (2019). Coastal semidiurnal internal tidal incoherence in the Santa Maria Basin, California: Observations and model simulations. *Journal of Geophysical Research: Oceans*, *124*, 5158–5179. https://doi.org/10.1029/2018JC014891

Lamb, K. G. (2014). Internal wave breaking and dissipation mechanisms on the continental slope/shelf. *Annual Review of Fluid Mechanics*, *46*, 231–254. https://doi.org/10.1146/annurev-fluid-011212-140701

Lentz, S. J., Elgar, S., & Guza, R. T. (2003). Observations of the flow field near the nose of a buoyant coastal current. *Journal of Physical Oceanography*, *33*, 933–943. https://doi.org/10.1175/1520-0485(2003)33<933:ootffn>2.0.co;2

Lentz, S. J., & Helfrich, K. R. (2002). Buoyant gravity currents along a sloping bottom in a rotating fluid. *Journal of Fluid Mechanics*, *464*, 251–278. https://doi.org/10.1017/s0022112002008868

Lentz, S. J., & Largier, J. (2006). The influence of wind forcing on the Chesapeake Bay buoyant coastal current. *Journal of Physical Oceanography*, *36*, 1305–1316. https://doi.org/10.1175/jpo2909.1

Lerczak, J. A., Barth, J. A., Celona, S., Chickadel, C., Colosi, J., Feddersen, F., et al. (2019). *Untangling a web of interactions where surf meets coastal ocean* (Vol. 100). https://doi.org/10.1029/2019EO122141

McPhee-Shaw, E. E., Siegel, D. A., Washburn, L., Brzezinski, M. A., Jones, J. L., Leydecker, A., & Melack, J. (2007). Mechanisms for nutrient delivery to the inner shelf: Observations from the Santa Barbara Channel. *Limnology & Oceanography*, *52*, 1748–1766. https://doi.org/10.4319/lo.2007.52.5.1748

McSweeney, J. M., Lerczak, J. A., Barth, J. A., Becherer, J., Colosi, J. A., MacKinnon, J. A., et al. (2020). Observations of shoaling nonlinear internal bores across the Central California Inner Shelf. *Journal of Physical Oceanography*, *50*(1), 111–132. https://doi.org/10.1175/JPO-D-19-0125.1

McSweeney, J. M., Lerczak, J. A., Barth, J. A., Becherer, J., MacKinnon, J. A., Waterhouse, A. F., et al. (2020). Alongshore variability of shoaling internal bores on the inner shelf. *Journal of Physical Oceanography*, *50*(10), 2965–2981. https://doi.org/10.1175/JPO-D-20-0090.1

Melton, C., Washburn, L., & Gotschalk, C. (2009). Wind relaxations and poleward flow events in a coastal upwelling system on the central California coast. *Journal of Geophysical Research*, *114*. https://doi.org/10.1029/2009jc005397

Oey, L.-Y., Winant, C., Dever, E., Johnson, W. R., & Wang, D.-P. (2004). A model of the near-surface circulation of the Santa Barbara Channel: Comparison with observations and dynamical interpretations. *Journal of Physical Oceanography*, *34*, 23–43. https://doi.org/10.1175/1520-0485(2004)034<0023:amotnc>2.0.co;2

Pineda, J. (1991). Predictable upwelling and the shoreward transport of planktonic larvae by internal tidal bores. *Science*, *253*, 548–549. https://doi.org/10.1126/science.253.5019.548

Relvas, P., & Barton, E. D. (2002). Mesoscale patterns in the Cape Sao Vicente (Iberian Peninsula) upwelling region. *Journal of Geophysical Research*, *107*, 21–28. https://doi.org/10.1029/2000jc000456

Relvas, P., & Barton, E. D. (2005). A separated jet and coastal counterflow during upwelling relaxation off Cape São Vicente (Iberian Peninsula). *Continental Shelf Research*, *25*, 29–49. https://doi.org/10.1016/j.csr.2004.09.006

Scotti, A., Butman, B., Beardsley, R. C., Alexander, P. S., & Anderson, S. (2005). A modified beam-to-earth transformation to measure short-wavelength internal waves with an acoustic Doppler current profiler. *Journal of Atmospheric and Oceanic Technology*, *22*, 583–591. https://doi.org/10.1175/JTECH1731.1

Send, U., Beardsley, R. C., & Winant, C. D. (1987). Relaxation from upwelling in the coastal ocean dynamics experiment. *Journal of Geophysical Research*, *92*, 1683–1698. https://doi.org/10.1029/jc092ic02p01683

Shanks, A. L., & Shearman, R. K. (2009). Paradigm lost? Cross-shelf distributions of intertidal invertebrate larvae are unaffected by upwelling or downwelling. *Marine Ecology Progress Series*, *385*, 189–204. https://doi.org/10.3354/meps08043

Suanda, S. H., Kumar, N., Miller, A. J., Di Lorenzo, E., Haas, K., Cai, D., et al. (2016). Wind relaxation and a coastal buoyant plume north of Pt. Conception, CA: Observations, simulations, and scalings. *Journal of Geophysical Research: Oceans*, *121*, 7455–7475. https://doi.org/10.1002/2016JC011919

Washburn, L., Fewings, M. R., Melton, C., & Gotschalk, C. (2011). The propagating response of coastal circulation due to wind relaxations along the central California coast. *Journal of Geophysical Research*, *116*. https://doi.org/10.1029/2011jc007502

Wing, S. R., Botsford, L. W., Largier, J. L., & Morgan, L. E. (1995). Spatial structure of relaxation events and crab settlement in the northern California upwelling system. *Marine Ecology Progress Series*, *128*, 199–211. https://doi.org/10.3354/meps128199

Wing, S. R., Botsford, L. W., Morgan, L. E., Diehl, J. M., & Lundquist, C. J. (2003). Inter-annual variability in larval supply to populations of three invertebrate taxa in the northern California Current. *Estuarine, Coastal and Shelf Science*, *57*, 859–872. https://doi.org/10.1016/s0272-7714(02)00416-x

Woodson, C. B., Washburn, L., Barth, J. A., Hoover, D. J., Kirincich, A. R., McManus, M. A., et al. (2009). Northern Monterey Bay upwelling shadow front: Observations of a coastally and surface-trapped buoyant plume. *Journal of Geophysical Research*, *114*. https://doi.org/10.1029/2009jc005623

Yankovsky, A. E., & Chapman, D. C. (1997). A simple theory for the fate of buoyant coastal discharges. *Journal of Physical Oceanography*, *27*, 1386–1401. https://doi.org/10.1175/1520-0485(1997)027<1386:astftf>2.0.co;2